

The Pennsylvania State University

The Graduate School

Department of Materials Science and Engineering

**PZT THIN FILMS FOR PIEZOELECTRIC MEMS  
MECHANICAL ENERGY HARVESTING**

A Dissertation in

Materials Science and Engineering

By

Charles Yeager

© 2015 Charles Yeager

Submitted in Partial Fulfillment

of the Requirements

for the Degree of

Doctor of Philosophy

May 2015

## ABSTRACT

This thesis describes the optimization of piezoelectric  $\text{Pb}(\text{Zr}_x\text{Ti}_{1-x})\text{O}_3$  (PZT) thin films for energy generation for by mechanical energy harvesting, and self-powered micro-electro-mechanical systems (MEMS). For this purpose, optimization of the material was studied, as was the incorporation of piezoelectric films into low frequency mechanical harvesters.

A systematic analysis of the energy harvesting figure of merit was made;. As a figure of merit  $(e_{31,f})^2/\epsilon_r$  (transverse piezoelectric coefficient squared over relative permittivity) was utilized. PZT films of several tetragonal compositions were grown on  $\text{CaF}_2$ ,  $\text{MgO}$ ,  $\text{SrTiO}_3$ , and  $\text{Si}$  substrates, thereby separating the dependence of composition on domain orientation. To minimize artifacts associated with composition gradients, and to extend the temperature growth window, PZT films were grown by metal organic chemical vapor deposition (MOCVD) for this experiment. Using this method, epitaxial  $\{001\}$  films achieved  $c$ -domain textures above 90% on single crystal  $\text{MgO}$  and  $\text{CaF}_2$  substrates. This could be tailored via the thermal stresses established by the differences in thermal expansion coefficients of the film and the substrate. The  $\langle 001 \rangle$  single-domain  $e_{31,f}$  for PZT thin films was determined to exceed  $-12 \text{ C/m}^2$  in the tetragonal phase field for  $x \geq 0.19$ , nearly twice the phenomenologically modeled value. The utilization of  $c$ -domain PZT films is motivated by a figure of merit above  $0.8 \text{ C}^2/\text{m}^4$  for (001) PZT thin films. Increases to the FoM via doping and hot poling were also quantified; a 1% Mn

doping reduced  $\epsilon_r$  by 20% without decreasing the piezoelectric coefficient. Hot poling a device for one hour above 120 °C also resulted in a 20% reduction in  $\epsilon_r$ ; furthermore, a 1% Mn doped film still reduced  $\epsilon_r$  by another 12% upon hot poling.

Two methods for fabricating thin film mechanical energy harvesting devices were investigated. It was found that phosphoric acid solutions could be used to pattern MgO crystals, but this was typically accompanied by damage to the PZT film. An energy harvester was fabricated by etching the MgO substrate down to 10-20  $\mu\text{m}$  under a circular diaphragm device; this structure had a natural frequency of 2.7 kHz and was estimated to provide a maximum RMS power of  $8.8 \mu\text{W}/\text{cm}^2 \cdot \text{g}^2$ . Due to the lack of selectivity in the patterning, MgO was not as versatile as silicon substrates, which can be etched rapidly by wet and dry methods.

To viably successfully release a PZT film onto a polymer passive elastic layer, dry (gas) etch methods were required preferable. This prevented etching of protected the interfacial bonding between PZT films and Parylene. A  $2 \text{ cm}^2$  thin film membrane (15  $\mu\text{m}$  Parylene/ 3  $\mu\text{m}$  Cyclotene 4022/ 0.1  $\mu\text{m}$  Pt-Ti/ 1.4  $\mu\text{m}$  PZT (52/48)/ 0.14  $\mu\text{m}$  Pt-Ti/ 1  $\mu\text{m}$   $\text{SiO}_2$ ) was released from a silicon substrate and operated with a 5 Hz natural frequency, the lowest reported for a thin film energy harvester operating in resonant excitation. Though problems existed with buckling of the beam due to tension in the Cyclotene 4022 (a benzocyclobutene, BCB, resin, BCB) from curing on a silicon substrate, the cantilevered device was calculated to output up to RMS  $0.53 \mu\text{W}/\text{cm}^2$  when swept through an arc  $>30^\circ$ . Silicon substrates facilitated scaling in size and quantity of devices compared to MgO substrates, which motivated an investigation in

chapter 5 into the reduction of  $90^\circ$  domain walls for thin films released from substrate clamping conditions.

Circular test structures were designed to produce systematic changes in the clamping condition of  $\{001\}$  PZT thin films. The stiffness of the substrate interface was modified either by using a PZT buffer layer on the substrate or by removing the substrate completely. Films allowed to stress relax upon release, via curling, had reduced domain wall restoring force compared to fully clamped structures, leading to a 72% increase in irreversible domain wall contributions for free-standing  $300\ \mu\text{m}$  features. The irreversible dielectric Raleigh coefficient,  $\alpha$ , for a  $1.64\ \mu\text{m}$   $\{001\}$  PZT film measured at 20 Hz increased from 40 kV/cm to 71 kV/cm in this way.

Griggio et al. reported  $\alpha$  of 148 kV/cm at 100 Hz for partially electroded broken sections of  $70\ \mu\text{m}$  diaphragms.<sup>131128</sup> To understand the relationship between the  $\alpha$  reported in those experiments and the results of this thesis, the size dependence of  $\alpha$  was investigated by partitioning  $300\ \mu\text{m}$  diaphragms into wedges. Both  $\alpha$ , and the dispersionfrequency dispersion of  $\alpha$ , increased as the membrane was sub-sectioned. This was attributed to, owing to a decrease in the elastic restoring force for  $90^\circ$  domain walls. Interface (local) stresses were found to have no significant smaller impact on domain wall mobility, even after the domain structure was annealed above the Curie temperature post release. This settles a debated question regarding the relative importance of locally induced stress compared to stress in the bulk.

## TABLE OF CONTENTS

LIST OF FIGURES.....	iv
LIST OF TABLES.....	xi
ACKNOWLEDGEMENTS.....	xii
Chapter 1 Introduction and Goals.....	1
1.1 Introduction	
1.2 Statement of Problem	
Chapter 2 Background	
2.1 Wireless Sensor Networks	
2.2 Piezoelectric Vibration Energy Harvesting	
2.3 The Properties of Ferroelectric PZT	
Chapter 3 Fabrication and Characterization of a Low Frequency PZT MEMS Energy Harvester	
3.1 Introduction	
3.2 Processing Development and Procedures	
3.3 Energy Generation and Mechanical Characteristics	
3.4 Conclusions	
Chapter 4 Dependence of Domain State and Film Composition on the Figure of Merit	
4.1 Introduction	
4.2 Experimental Procedure	
4.3 Results and Discussion	
4.3.1 Piezoelectric Coefficient as a Function of <i>c</i> -Axis Fraction	

### 4.3.2 Figure of Merit Dependence on Domain State

## 4.4 Conclusions

## Chapter 5 Mobility of Domain Walls in Released PZT Thin Films

### 5.1 Introduction

### 5.2 Experimental Procedure

#### 5.2.1 Thin Film Deposition

#### 5.2.2 Test Structure Fabrication

#### 5.2.3 Electrical Characterization

### 5.3 Results and Discussion

#### 5.3.1 Polarization Switching

#### 5.3.2 Rayleigh Law Behavior

#### 5.3.3 Piezoelectric Coefficient for Membranes

### 5.4 Conclusions

## Chapter 6 Conclusions and Future Work

### 6.1 Conclusions

### 6.2 Future Work

#### 6.2.1 Domain Wall Back-Switching In Thin Films

#### 6.2.2 Thin Film Transfer From Silicon Substrates

#### 6.2.3 Integrated ZnO TFT Electronics on PZT Devices

## Appendix A Thin Film Composites For Energy Harvesting

## REFERENCES

## LIST OF FIGURES

Figure 2-1: Attractive network topologies for WSNs achieved using the ZigBee protocol.....	5
Figure 2-2. A vibrational mode shape of the Golden Gate Bridge captured using a SHM WSN...	6
Figure 2-3. Integrated microprocessor and 2.4 GHz radio modules from Human++ program.....	7
Figure 2-4. Schematic of a vibration energy harvester after William and Yates with seismic mass $m$ , a spring with stiffness $k$ , and transducer as damping $d$ , displacement of the mass and base are $z$ and $y$ respectively.....	10
Figure 2-5. Two port model of a transducer, the product of the across ( $A$ ) and through ( $T$ ) variables at a port give the energy stored there. The variables are labeled with the example of an electromechanical transducer. ....	12
Figure 2-6. The square area enclosed by a point on the diagonal line is proportional to the value $U_{out}$ ; this is maximized in the state shown by the grey box and demonstrates the importance of matching the load impedance to the transducer output port for any transducer system. ...	13
Figure 2-7. Comparison of the FoM and $e_{31,f}$ coefficient for piezoelectric thin films which have been suggested for energy harvesting. The FoM for PZT films may range from 0.05–1.5 $C^2/m^4$ based on deposition conditions such as substrate and film orientation. Data taken from references.....	16
Figure 2-8. Filtered acceleration versus time of a subject walking on a treadmill (left) and the resulting Fourier transform (right) showing the distribution of vibration energy.....	20
Figure 2-9. A wide-band MEMS energy harvester using a Duffing stiffening bridge design.....	21
Figure 2-10. Gibbs free energy profiles calculated by Landau-Ginsburg-Devonshire theory. Polarization rotation is favorable between polar phases (T–R), while polarization extension is favorable between a polar and non-polar phase (T–C, R–C).....	24

Figure 2-11. Domain walls found tetragonal PZT, 180° wall (left) and 90° wall (right).....26

Figure 2-12. Representation of local potential energies encountered by mobile domain walls.  
Wall motion is irreversible if the wall does not return to its initial position.....28

Figure 3-1. XRD spectra of CVD PZT films with  $x=0.19$  (left) and  $x=0.43$  (right). Substrates from top to bottom on left are:  $\text{CaF}_2$ ,  $\text{MgO}$ ,  $\text{SrTiO}_3$ , and  $\text{Si}$ , on right:  $\text{MgO}$ ,  $\text{Si}$ , and  $\text{Si}$  (sol-gel PZT). At 400 °C these substrates have thermal expansion values of 28.4 ppm/K, 13.6 ppm/K, 11.2 ppm/K, and 3.9 ppm/K, respectively. LNO =  $\text{LaNiO}_3$ , STO =  $\text{SrTiO}_3$ , BST =  $\text{Ba}_{1-x}\text{Sr}_x\text{TiO}_3$ .....  
37

Figure 3-2. XRD scan of PZT 200 & 002 peaks for PZT on Si with  $x = 0.19$  (left) and PZT 400 & 004 peaks for PZT on Si with  $x = 0.43$  (right). The enhanced splitting of the 400 peak was required to assess  $f_{001}$  for the sol-gel film on Si due to the much larger peak width than the MOCVD films making fits uncertain when 200/002 peaks were employed.....37

Figure 3-3. Cross sections of MOCVD PZT films showing representative microstructure differences between: epitaxial films on single crystals (a-d), fiber-textured PZT on Si (e -f), and films with Pt layers (a-b) compared to oxide-only layers (c-d). The compositions are: a)  $x = 0.19$ , b)  $x = 0.43$ , c)  $x = 0.29$ , d)  $x = 0.37$ , e)  $x = 0.37$ , f)  $x = 0.29$ .....38

Figure 3-4. PZT lattice parameters determined by four-circle XRD measurements (left) as a function of  $[\text{Zr}]$  compared to the bulk ceramic (dashed line); bars show 95% confidence limits. XRD scans (right) showing out-of-plane reflections stacked by increasing  $[\text{Zr}]$ , dashed lines are guides to the eye, showing the trend in peak position.....40

Figure 3-5. Volume fraction of  $c$ -domains for  $\{001\}$  PZT films grown on  $\text{Si}$ ,  $\text{SrTiO}_3$ ,  $\text{MgO}$  and  $\text{CaF}_2$  (the same symbols are used throughout to denote the substrate). CVD films with  $x = 0.19$  were grown at 625 °C while other CVD films were grown at 500 °C, a color code is used throughout to denote composition. A dagger (†) indicates weak 110-PZT peaks were

present and accounted for in calculating  $f_{001}$ . A double-dagger (‡) denotes samples prepared by sol-gel.....41

Figure 3-6. Linear change in dielectric constant and  $e_{31,f}$  of poled sol-gel {001}PZT 48/52 films crystallized at 650 °C (950 K) on silicon, SrTiO<sub>3</sub> and MgO substrates as a function of the calculated thermal strain.....42

Figure 3-7. Thermal expansion coefficient,  $\alpha(T)$ , for PZT and substrates. The colored areas are equal to the thermal strains at  $T_C$  used in Figure 4-6 which are calculated by the integral: .....43

Figure 3-8. Measured dielectric constants of poled films versus  $f_{001}$ . The solid line shows calculations from phenomenology for the dielectric susceptibility of mixed  $c/a$  domain state. The films match the prediction particularly when  $f_{001} > \sim 80\%$ .....44

Figure 3-9. Dielectric constant versus bias field for epitaxial {001}PZT 52/48 films with and without Mn doping. The lower un-biased permittivity of the Mn-doped films increased the (hot poled) FoM by 20%.....45

Figure 3-10.  $e_{31,f}$  versus  $c$ -axis texture for tetragonal PZT films.  $R^2$  for the line of best fit through the origin is given with the extrapolated value of  $e_{31,f}$ . Vertical bars show one standard deviation in the measured data. Uncertainty in the slope is the 90% confidence interval....46

Figure 3-11. Experimentally derived intrinsic [001]  $e_{31,f}$  from Figure 4-10 and from phenomenology (dotted line). Measured values of  $a$ -domain {100} PZT films on silicon by Lederman et al. (2001) for comparison. ....48

Figure 3-12. Average FoM for tetragonal compositions of PZT films. Vertical bars indicate one

standard deviation in the calculated value.....	49
Figure 4-1. Relative XRD intensity of Pt on (100)MgO substrates sputtered under a matrix of conditions to increase adatom mobility. The introduction of O <sub>2</sub> (g) significantly reduces the 111 peak intensity in favor of 200 oriented Pt. Only films grown at 750 °C were as well textured as MOCVD grown (100) Pt received from collaborators. The unlabeled peaks are due to numerous tungsten lines generated by this X-ray source.....	54
Figure 4-2. Process flow for D-cantilever on MgO transferred to Parylene.....	60
Figure 4-3. (1) Device backside before complete MgO etch (2) Pt/PZT detaches from Parylene immediately upon exposure, even tearing away from the Pt region which remains flat (3) after all MgO has been etched, Pt/PZT/Pt and Pt/PZT regions have buckled off the Parylene (which remains stretched flat), the Pt boarder also remains flat.....	61
Figure 4-4. Figure 4-4. Upper Row: (1) Parylene side of 1×1 cm test sample (2) SRO side of test membrane (3) the membrane deforms upward but does not crack (drying rings are seen) Lower Row: (4) The back of a fully (MgO) etched D-cantilever shows homogenous fracturing in the PZT beam and the end mass has fallen away (5) SEM of fractured Pt/PZT/ SRO beam. ....	62
Figure 4-5. Figure 4-5. Pt/PZT/Pt stack fabricated with single RIE mask to avoid mis-alignment. The large deformation of released segments conclusively shows the Parylene interface can never be exposed to the wet etch.....	64
Figure 4-6. A diaphragm clamped at the perimeter will necessarily have an inflection point in stress for which the electrode arrangement must be designed. Image from Ref[123] .....	65
Figure 4-7. The process flow for fabricating diaphragms had four steps, Pt/Ti top electroding was followed by 10 μm Parylene deposition. After plasma etching the parylene on the back, the MgO was wet etched. An end mass and contact wires were added after MgO etch.....	67

Figure 4-8. A process flow energy harvesting devices fabricated from a PZT stack on a silicon substrate. Both surface and cross-section views are given alongside a photo of the device at the particular step.....70

Figure 4-9. (1) Parylene results in a weak interface, which a: 110 nm Pt-Ti/ 2  $\mu\text{m}$  PZT/ 250 nm LNO/ 100 nm SiO<sub>2</sub> stack curls away from to relax stress (2) a dry film resist causes the greatest amount of curling and was not viable.....72

Figure 4-10. (1) Schematic of PEH test bed, a device is excited (with a shaker table or by a single impulse) and is connected to an oscilloscope with a 1 M $\Omega$  input impedance, the device is also connected to a resistive load which is varied to match the device impedance (2) An accelerometer is placed between the device and the shaker with outputs sent to the oscilloscope.....73

Figure 5-1. XRD for the {001} textured PZT films: a 30 nm Pt electrode between layers of PZT had only minimal impact on the degree of {001} texture. The single layer film is 1.17  $\mu\text{m}$ , the 1.64  $\mu\text{m}$  film was obtained by depositing an additional 5 layers on a portion of that substrate.....79

Figure 5-2. FESEM showing surface and cross-section for three PZT structures investigated. Thicknesses were a. 1.17  $\mu\text{m}$ , b. 1.64  $\mu\text{m}$ ; c. the bi-layer PZT film was 1.04  $\mu\text{m}$  thick above the buried electrode and 0.60  $\mu\text{m}$  below. The black segments denote 0.5  $\mu\text{m}$ .80

Figure 5-3. **Upper Row:** (1) Mask design for locally released membrane (2) Released “flat” membrane, no substrate clamping though no deformation (3) Material was sometimes seen to be redeposited on resist walls (4) Membrane cleared away revealing silicon etch pits **Middle Row:** (1) Mask design for globally released (relaxed) membrane (2) Released ‘tabs’ relaxed downward and were free to deform when probed (3) Cracking of the undercut film concentrated at tight curvatures **Lower Row:** (1) Mask design for relaxed bridge with

uniaxial strain gauge (2) The uniaxially released bridges curl along the width to relax stress and are contacted via pads at both sides.....84

Figure 5-4. Wafer flexure method setup for strain and piezoelectric charge measurement. A pressure chuck flexes a carrier holding the sample. Probes connect to a strain measuring circuit (red) and charge measuring circuit (green).....86

Figure 5-5.  $P_r$  is compared for three release states: global & local, local only, and clamped. Globally released devices show an early increase in  $P_r$ ; clamped devices require larger fields to de-pin walls, but achieve equal or greater  $P_r$ . Annealing devices above  $T_C$  facilitated increase in  $P_r$  by depinning the aged films.....88

Figure 5-6. The Rayleigh parameters  $\epsilon_{init}$  and  $\alpha$  are shown for different release conditions. Local declamping has little effect but global declamping universally leads to a smaller irreversible response and nearly doubled (for thicker layers) irreversible contribution.....91

Figure 5-7 Effect of membrane deformation on the irreversible domain wall motion. Both  $\alpha$  and the level of dispersion increase as the restoring force for the membrane is reduced.....93

Figure 5-8. Indirectly-lit partitioned diaphragms, cracking extended to the boundary of the released region. One third of the electrode remained clamped (measured by camera software);  $\alpha$  for this region (Table VI) was separated as a linear mixing contribution.....94

Figure 5-9. The MEMS bridge structure measured the  $e_{31,f}$  of a released  $1.17 \mu\text{m}$  PZT film, the poling dependence was less steep than for a clamped (bi-layer) PZT film.....95

## LIST OF TABLES

Table I: On-Resonance Driven MEMS Devices in Literature.....	19
Table II: Sputter Conditions for (100) Pt.....	33
Table III: Substrates, [Zr] and Thicknesses of (001) PZT Thin Films used to Investigate the Influence of Domain State on Energy Harvesting Figure of Merit .....	35
Table IV. Example Neutral-Axis Calculation for a PZT/SiO <sub>2</sub> / & Polymer Cantilever.....	53
Table V. Dimensions and Natural Frequency for Cantilever Devices on MgO Device .....	58
Table VI. Dimensions of Diaphragm Devices.....	66
Table VI: ICP Etch Conditions for PZT and Pt.....	82
Table VII: Rayleigh Frequency Coefficients.....	92

## **ACKNOWLEDGMENTS**

## Chapter 1

### Introduction and Goals

#### 1.1 Introduction

Bryzek describes a possible near future called the “trillion sensor universe”, where low-cost micro-electromechanical systems (MEMS) perform supply chain tracking, health monitoring, infrastructure monitoring, and earth/climate monitoring. The more general idea of ubiquitous computing in everyday life, sometimes called the “internet of things”, was published by Weiser (1991) and implies networked smart devices with sensing and processing capabilities. Chapter 2 will begin with a survey on sensor networks.

Ongoing reduction in power requirements for MEMS sensors, radios, and microprocessors has motivated development of MEMS energy scavenging systems. The autonomy of self-powered systems eases limitations regarding accessibility (i.e. allowing remote and embedded deployment) and on the number of sensor nodes deployed. A motivation for mechanical energy scavenging is followed with the theory of piezoelectric transduction. The case for  $\text{PbZr}_{1-x}\text{Ti}_x\text{O}_3$  (PZT) MEMS energy harvesters is given through a review of the literature. Specific attention is paid to harvesting from motion of the human body. Analysis of human motions given in Chapter 2 guided the design and fabrication of a MEMS energy harvester, which is the subject of Chapter 4. The final two sections of Chapter 2 describe key properties of PZT related to energy generation. The significance of the property anisotropy in ferroelectrics is

discussed for this application. Chapter 2 concludes by providing context for Chapter 5 through a literature review of the quantitative role of substrate clamping to ferroelastic domain reorientation. Chapter 3 provides the experimental link of the domain state of PZT films to the maximum possible energy transduction.

## 1.2 Statement of Problem

One of the key goals of this thesis was to provide a better understanding of the structure-property relations governing PZT thin films for energy harvesting. Towards this end, the relationship between average domain orientation and piezoelectric coefficient in thin films was quantified. The fraction of *c*-domains in {001} films correlates with the energy generation factor due to the anisotropy in the intrinsic material properties. However, there is no complete experimental data set in the present energy harvesting literature to validate the modeled values for  $e_{31}f$  as functions of either the concentration of Zr or the *c*-domain fraction.

Piezoelectric thin films are widely utilized in MEMS devices, including resonant MEMS energy harvesters. To increase the power output, these devices are often excited at the natural frequency. For certain applications, such as harvesting energy from the human body, available MEMS harvesters resonate well above useful frequencies. This motivates motivated development of fabrication methodologies for low frequency MEMS energy harvesters in which a stiff passive elastic layer such as Si is replaced with a flexible polymer. The aim is to incorporate large-area PZT thin films into composite cantilevers with arbitrarily low natural

frequencies.

Given the significance of tailoring the domain configuration for energy generation applications, there is a need to understand the limits of domain reorientation in films released from the substrate. MEMS test structures were designed to compare the properties of clamped films to those with systematic changes in the mechanical boundary conditions.

## Chapter 2

### Background

#### 2.1 Wireless Sensor Networks

Wireless sensor networks (WSNs) use autonomous distributed sensors to gather information about an environment. Each member of the network, called a node (or mote) contains components for sensing, computing, communication, and power storage. Nodes may merely collect data to relay to a base station or may also combine data with adjacent nodes and perform substantial processing operations such as aggregation or actuation. WSNs may record information redundantly, making them robust against point failures compared to a single large sensor. Additionally, *ad hoc* networks capable of self-organizing after deployment will find the locations of all nodes and determine network topology.<sup>3</sup> In this way, WSNs may deploy without prior planning in dynamic environments. WSN-accessible data about ecosystems, infrastructure, homes, and even our bodies is expected to be of value in the age of big data.

##### *2.1.1 Progress in Sensor Network Technology*

Early developments in sensor network technology began in the 1950's in defense research. A system of hydrophones deployed in the Atlantic Ocean called the Sound Surveillance System (SOSUS) was developed to locate Soviet submarines. Undersea cables connected the

transducer arrays, which would triangulate submarine positions over hundreds of miles. In the 1980's the Distributed Sensor Network (DSN) program at the Defense Advanced Research Project Agency (DARPA) significantly expanded sensor network technology around a communication model similar to the Arpanet ARPAnet (the predecessor to the internet) with many spatially distributed low-cost nodes which collaborate. This resulted in advances in distributed computing, signal processing, tracking, and testbeds. In the 21<sup>st</sup> century, computer and communication technologies experienced unprecedented advancement. Inexpensive low-power microelectromechanical systems (MEMS) have reduced the sizes of sensors; while growing complexity of application specific integrated circuits (ASICS) has significantly increased computational resources while reducing power consumption for sensor nodes. In the early 2000's DARPA conducted the Sensor Information Technology program (SensIT). The focus was on developing new methods of networking, including a rapidly deployed *ad hoc* network, and utilizing the distributed computing paradigm to achieve timely data extraction and dynamic tasking of the network. In a vehicle tracking field test, six wireless sensor nodes were dropped from an unmanned aerial vehicle (UAV) and established an *ad hoc* network. Each mote sampled a 2-axis magnetometer at 5 Hz and filtered the data before transmitting the time-stamped event over a multi-hop path back to the UAV. This kind of low-latency, short-range, interactive WSN was soon pursued for applications other than the war fighter, such as networking sensors to automate and monitor home and businesses environments. The ZigBee network layer protocol was developed in the early 2000's for low-rate low-power wireless personal area networks. ZigBee offered additional advantages over Bluetooth or Wi-Fi by achieving a low error rate in environments with low signal to noise ratios and by enabling

desired network topologies (i.e. star, mesh, cluster tree). Figure 2-1 shows a sampling of the network topologies possible with the ZigBee protocol. Three members are identified in Figure 2-1: end-devices which may have full (i.e. routing) or reduced functionality (RFD), full functionality devices (FFD), and the network coordinator. Networks using ZigBee are capable of multi-hop routing, route discovery, and network joining/leaving and utilize 16-bit address naming (up to  $2^{16}$  nodes).<sup>9</sup>

Figure 2-1: Attractive network topologies for WSNs achieved using the ZigBee protocol.<sup>9</sup>

### *2.1.2 Applications for Wireless Sensor Networks*

The properties of WSNs suggest numerous applications, such as those for agriculture or collecting data about terrestrial and marine ecosystems. For example, Corke et al. developed a WSN consisting of soil moisture sensors and animal tracking sensors for the purpose of optimizing the density of cattle in a grazing area. Solar-powered sensors relayed time histories of the cattle's positions over a multi-hop path to a collection node. Additionally, Corke et al. deployed a WSN inside irrigation bores in the coastal Burdekin sugar cane growing region (Queensland, Australia). Over-extraction of water from the aquifer leads to saltwater intrusion; nine sensors were deployed to monitor salinity, water table level, and water extraction rate. Over 1.5 years, the network reported over a million readings. Corke et al. also reports on WSNs for assessing rainforest biodiversity, monitoring lake temperature profiles to predict algal blooms.

Albaladejo et al. (2010) have compared twelve oceanic WSNs projects; WSNs can collect data with much lower investment of time and money compared to high-performance equipment such as autonomous underwater vehicles. In 2012 the Shelburne Vineyard (Williston, VT) partnered with MicroStrain (Williston, VT) to deploy a WSN capable of monitoring temperature, relative humidity, soil moisture, leaf wetness, and solar radiation sensors across multiple locations. This system enabled the vineyard to better protect budding vines from springtime cold snaps as well as use water and fertilizer more efficiently for 5 acres of Marquette grapes.

Structural health monitoring (SHM) technology monitors the rate and severity of changes in the state of structures through detecting damage or changes in system behavior. It has been reported that WSN offers similar performance at a significantly reduced price to install and maintain compared to wired sensor systems. Kim et al. (2007) reports on a prototype WSN tested on the Golden Gate Bridge in San Francisco Bay. This system was highly scalable. Up to 46-hops relayed data to the base station, but by pipelining the data, a bandwidth above 440 B/s was maintained. The time synchronized high-frequency sampling of the four accelerometers provided SHM data about the bridge. Figure 2-2 shows one of the bridge's mode shapes captured by the sensors compared to two calculated shapes.

Figure 2-2. Anti-symmetric vertical mode shape of the Golden Gate Bridge captured using a SHM WSN.

Another application which benefits heavily from complementary advances in MEMS sensor technology and increases in the computational and storage capabilities of smartphones is that of medical sensing and health monitoring. Unobtrusive wearable or implanted wireless

sensors form the subject of rapidly growing research into the body sensor network (BSN). The radio in a BSN may not need to transmit a long distance. This is key, as large power systems will be cumbersome to wear. This motivates reduction in power consumption and makes BSNs comparatively resource limited. Among several health monitoring systems that have been developed is the Human++ program at the Holst Centre. The program has demonstrated several platforms, one acquires electroencephalograph, electrocardiogram, and electromyograph signals then transmits them to a personal device while consuming less than 1 mW average power. This is achieved by duty cycling the radio (which consumes 90% of the power when on) to only a few percent. Additionally, a microprocessor and wireless radio integrated into a smart band-aid one tenth the size of a credit card as a 2-D platform for future generations of sensors marks an evolution from previous 3-D modules. Figure 2-3 compares the 3-D and 2-D prototype wireless sensor nodes developed in this program.

Figure 2-3. Integrated microprocessor and 2.4 GHz radio modules from the Human++ program.

16

Another platform which has been researched widely is sensors built into clothes, such as the MyHeart project. This work embedded electrodes and microcircuits into textiles to make an unobtrusive sensor which collects an ECG signal. Embedded low-power digital signal processing was demonstrated to enhance the ECG signal, which becomes degraded from motion artifacts due to the variable skin-electrode interface. Overall, the use of autonomous wireless sensors for

health care is expected to significantly improve quality of life for chronically ill patients. Medication compliance may be improved, such as for patients with hypertension by monitoring blood pressure. Diabetic persons may be able to monitor blood sugar to avoid hypoglycemia, or asthmatics may be able to sense local concentrations of air pollutants such as ozone to assess respiratory risks in real-time.<sup>14</sup>

### *2.1.3 Power Limitations of Autonomous Wireless Sensors*

For systems which receive power only from batteries, there is a tradeoff between the lifetime of the node and the resources available for sensing, computation, and communication. In the case of the prototype WSN for SHM which was deployed on the Golden Gate Bridge, each node was equipped with four 9 V lantern batteries. Each sampling by the sensor network involved time-stamp synchronization, a simultaneous collection event by each node, and transmission of 20 MB of data in total. Each sampling process took nine hours and only 13 sets of data were collected during the lifetimes of the initial deployment of batteries. This places practical limitations on the number of nodes. Desire to reduce the size of power systems and increase battery life has motivated significant research into more power efficient radios and microprocessors as well as optimized operating systems and communication protocols. Aggressive duty cycling is often employed, with nodes spending long periods in idle low-power states. As the node becomes more difficult to access (is as the case for a surgically implanted device) the cost and challenges associated with replacing batteries becomes more prohibitive. This has resulted in a focus on harvesting sources of ambient energy such as solar, wind, thermal, and mechanical for WSNs. Generally, outdoor applications such as civil and agricultural ones

favor solar energy due to the higher power levels available, while BSNs for health monitoring have mainly explored thermal and mechanical energy that is generated by the human body. A comparison of the relative merits of various power sources is reviewed by several authors and is not in the scope of this chapter.’

## **2.2 Piezoelectric Vibration Energy Harvesting**

Piezoelectric materials exhibit several advantages as a transducer for energy harvesting compared to electromagnetic and electrostatic generators. If electromagnetic dynamos are scaled to small dimensions (e.g. sub cm) then the output voltage may become too low for use.<sup>21</sup> While electrostatic generators perform well in MEMS scale devices, they require a priming charge from a power supply which may not be available for many applications. Piezoelectrics however, can output electric energy at several volts and have a high energy density, making them ideal for MEMS energy harvesters.

### *2.2.1 Theory of the Harmonic Oscillator and Linear Transducer*

Some of the first researchers to investigate piezoelectric energy harvesting were Williams and Yates (1996). They describe an inertial generator consisting of a seismic mass,  $m$ , connected to a spring with stiffness,  $k$ , and the transducer as a damping element,  $d$ , attached at one point to a vibrating body. Figure 2-4 shows their schematic of a vibration harvester.

Figure 2-4. Schematic of a vibration energy harvester after William and Yates with seismic mass  $m$ , a spring with stiffness  $k$ , and transducer as damping element  $d$ , displacement of the mass and base are  $z$  and  $y$  respectively.

They used a lumped-parameter equation of motion for a harmonic oscillator (2.1) to describe the system. This model produces accurate results, especially if the mass is concentrated.

(2.1)

For the exact treatment, which includes the moment forces introduced by a distributed mass, the Euler-Bernoulli equation must be used. Even so, lumped-parameter equations are often used in the literature to model the power produced by a cantilever beam vibrating at resonance.' In the same year, Umeda et al. (1996) published work on the transduction of vibrations generated by dropping a steel bearing on a piezoelectric plate. Noticing that the transducer dissipated more electric energy when less kinetic energy was returned to the bearing; they concluded the mass should be fixed to the plate so as not to rebound. They proposed a widely cited equivalent circuit for a piezoelectric energy harvester and modeled power output as functions of the mechanical quality factor, coupling coefficient, dielectric loss, and load resistance.

Roundy et al. (2005) provided a general expression for the maximum power extractable from a linear transducer. This method derives the maximum power via a transmission coefficient,

$\lambda = U_{\text{out}}/U_{\text{in}}$ , multiplied by the time derivative of the energy put into the system,  $dU_{\text{in}}/dt$  (which is equal to  $\omega U_{\text{in}}$  for sinusoidal vibrations).

(2.2)

The expressions for  $\lambda_{\text{max}}$  and  $U_{\text{in}}$  are derived from the constitutive equations for a linear transducer (2.3), which can be shown conveniently in matrix form.

(2.3)

The  $A_1$  and  $A_2$  are the across variables (measured “across” the element, e.g. voltage),  $T_1$  and  $T_2$  are the through variables (measured “through” the element, e.g. current), and  $q_{ij}$  are proportionality constants. A dynamic system coupling two phenomena has a minimum of two ports which describe the system by what is measured at each port. Multiplying the across and through variables at a given instant results in the power stored in the element. A transducer has two sets of across and through variables describing its two domains (e.g. electrical and mechanical). Figure 2-5 illustrates a model for a two port transducer after Bright (2001).<sup>29</sup>

Figure 2-5. Two port model of a transducer, the product of the across ( $A$ ) and through ( $T$ ) variables at a port give the energy stored there. The variables are labeled with the example of an electromechanical transducer.<sup>29</sup>

For the electric variables, voltage is across the transducer while current is the through

variable. For the mechanical variables, velocity is observed across the transducer while force is the through variable. The coupling coefficient is defined as the energy stored at the output port (with no load) over the energy at the input port and depends only on the proportionality constants. The general form of the coupling coefficient for a linear transducer is defined in equation 2.4.<sup>28</sup>

$$(2.4)$$

The values for  $U_{in}$  and  $U_{out}$  are calculated by holding the across variable constant and integrating with respect to the through variable. Substituting in the expression for the across variables  $A_1$  and  $A_2$  from equation 2.3 yields a value for  $\lambda = U_{out}/U_{in}$  which is dependent upon the through variables  $T_1$  and  $T_2$ , and the across variable  $A_2$  (the voltage and current,  $V$  and  $I$ , at the output port). This demonstrates the importance of choosing the correct load to match a piezoelectric energy harvester. A similar method was used by Wang et al. (1999) to show that a mechanical load must be optimally matched to transfer maximum power from a bimorph given an electrical input. Roundy et al. show graphically (Figure 2-6) how transmitted power to a load falls to zero for the states:  $(A_2=0, T_2=T_{20})$  and  $(A_2=A_{20}, T_2=0)$ . They also demonstrated that  $U_{out}$  is maximum for the load which generates the state  $(\frac{1}{2}A_{20}, \frac{1}{2}T_{20})$ .

Figure 2-6. The square area drawn from a point on this diagonal (the grey box) is proportional to the power transfer value  $U_{out}$ ; this is maximized in the state is aximum transfer is shown by the

grey box. Changing the load on the output port moves the point along the line. Impedance matching is done to select the maximum power transferred.

Using equation 2.4 and  $\lambda_{\max} = U_{\max} / U_{\text{in}}$ , Roundy et al. gives  $\lambda_{\max}$  as a function of the system coupling coefficient, see equation 2.5. Evaluating 2.5 for a transducer with 100% coupling efficiency ( $k^2=1$ ) places an upper bound on  $\lambda_{\max}$  of  $\frac{1}{2}$ . Therefore, to increase the power output from a transducer, it is important to make  $\lambda_{\max}$  large by maximizing the coupling coefficient as well as designing the load to maximize the actual average transmission coefficient.<sup>28</sup>

(2.5)

The constitutive equations for piezoelectricity (2.6) can be inserted into 2.4, where  $S$  is strain,  $D$  is dielectric displacement,  $s$  is compliance,  $d$  is the piezoelectric coefficient,  $\epsilon$  is permittivity,  $T$  is stress, and  $E$  is electric field, yield the piezoelectric coupling coefficient (2.7)

(2.6)

(2.7)

The maximum power can be given for a piezoelectric transducer as a function of material property and vibration input variables. The AC magnitude of the seismic force on the piezoelectric,  $F$ , is written as  $F = Q A a$ , where  $Q$  is the total quality factor of the resonator and  $A$  is the acceleration. Substituting 2.5 and the expression for  $U_{\text{in}}$  into 2.2 yields the maximum power

extractable from a face-loaded transducer (2.8).<sup>28</sup>

(2.8)

This equation can be made more useful for the purpose of MEMS energy harvester design by writing out the terms inside the coupling coefficient. In this case the  $e_{31,f}$  coefficient is used. This coefficient defined in equation 2.9 relates charge displacement to the biaxial strain state,  $x_1+x_2$ .

(2.9)

A variant of equation 2.8 which shows the maximum power available for a fixed displacement, and inserts the materials terms in the coupling coefficient is given as equation 2.10. Note the frequency dependence changes from inverse to cubic by fixing the displacement.<sup>24,31</sup>

(2.10)

Equation 2.10 provides a useful view of the impact each material property has on the generated power. For MEMS energy harvesters with thin film piezoelectric layers, the substrate stiffness often dominates the effective mechanical properties of the device.<sup>38</sup> In this case, only the piezoelectric coefficient and the permittivity influence the power generation. Furthermore, different piezoelectric materials can be compared quantitatively by isolating these terms in equation 2.10. This is known as the figure of merit for MEMS energy harvesting and is used as a metric for choosing between materials. The figure of merit, not including the permittivity of free space, is given in equation 2.11.

(2.11)

This metric is the focus of Chapter 3, which is concerned with defining the bounding values of the FoM for lead zirconate titanate thin films.

### 2.2.2 Review of Materials for Piezoelectric MEMS Energy Harvesting

Piezoelectric energy harvesting devices have been proposed using materials including thin films, thick ceramic films/fibers, polymers, and single crystals.” The FoM given in 2.11 only compares materials for thin film energy harvesting devices with top and bottom electrodes, which is the focus of this work. There are two general families of materials commonly used for this purpose. One is the wurtzite structured piezoelectrics, AlN and ZnO, which benefit from well understood deposition technology but do not have the largest FoM. The second is the perovskite ferroelectrics,  $\text{Pb}(\text{Zr}_x\text{Ti}_{1-x})\text{O}_3$ ,  $(\text{K}_x\text{Na}_{1-x})\text{NbO}_3$ , and  $\text{BiFeO}_3$ , which have the highest reported FoM. However, in many cases the superior FoM may not necessarily be achieved. A comparison of the FoM for many thin films proposed for energy harvesting is given in Figure 2-7 after Trolier-McKinstry et al. (2011).

Figure 2-7. Comparison of FoM and  $e_{31,f}$  of piezoelectric films for energy harvesting, FoM for PZT ranges  $0.05\text{--}1.5 \text{ C}^2\text{m}^{-4}$  based on substrate and orientation. References [ , , , , , , , ].

It can be seen that AlN is superior to the randomly textured PZT films, which were the state-of-the-art before texture control was introduced, circa 2001.<sup>36</sup> The demonstration of higher

piezoelectric coefficients due to a newly discovered phase transition between hexagonal AlN and rocksalt ScN by Akiyama et al. (2009) further increased the FoM for (Sc,Al)N beyond the then-available PZT materials. Shortly after, Wasa et al. (2009, 2012) and Trolier-McKinstry et al. (2011) suggested epitaxial (001)PMnN-PZT and (001)PZT thin films grown on (100)MgO substrates at  $>500$  °C for energy harvesting.<sup>46,37</sup> The best sputtered PZT films on MgO had strongly depressed dielectric constants of 100 and yielded the highest reported FoM, though the film-to-film reproducibility of  $e_{31,f} > -10$  C/m<sup>2</sup> was inconsistent. The suitability of PZT films on high thermal expansion substrates for energy harvesting of PZT films on high thermal expansion substrates, such as MgO, Ni, and CaF<sub>2</sub>, has since been reported by several groups, including by the author.<sup>48,44,45</sup> These studies confirmed that compressive stress in the PZT films can be used to reduce the permittivity and increase the figure of merit for energy harvesting.

The decision of material choice must also take into account the feasibility of processing the piezoelectric. The restriction of hazardous lead in electronics, as well as the relative difficulty depositing a three-cation thin film (PZT) has made AlN appealing commercially, especially since the deposition technology for AlN is well established due to the market for FBAR devices. For example, MicroGen Systems (Rochester, NY) offers a product line of MEMS energy harvesters utilizing AlN thin films. For high-performance applications, PZT can produce a superior FoM. PZT is readily produced on 4" or 6" silicon wafers but is currently not superior to (Sc,Al)N, while PZT grown on single crystals is difficult to fabricate into devices, though methods to transplant the film to a secondary substrate have been demonstrated.<sup>48</sup> Nonetheless, several

bulk/thick-film commercial PZT energy harvesters are available such as the Vulture bimorph using ceramic wafers by Midé (Medford, MA), piezoelectric fiber composite (PFC) harvesters sold by Advanced Cerametrics (Lambertville, NJ), and screen printed PZT cantilevers produced by Meggitt (Christchurch, UK). These devices have the advantage over (Sc,Al)N in that the piezoelectric layer is up to hundreds of microns thick. These devices compete with (relatively) larger and heavier electromagnetic vibration energy harvesters, such as those produced by Perpetuum. These devices produce tens of milli-watts power and operate at 0.025 g.

### *2.2.3 Review of Piezoelectric MEMS Energy Harvesting Devices*

The first piezoelectric MEMS vibration harvester was reported by Jeon et al. (2005) and was based on the in-plane polarization mode introduced by Bernstein et al. (1999).<sup>9</sup> An interdigitated electrode (IDE) pattern, used by Bernstein et al. to increase the voltage sensitivity of a 2D ultrasound array, increased the output voltage up to 2.4 V. Low output voltage is problematic for vibration harvesting, since the AC signal must be rectified and the small forward bias of the rectifying diodes ( $< 0.2$  V) must be exceeded. The device by Jeon et al. dissipated 1  $\mu$ W into a 5.2 M $\Omega$  load at a vibration input of 105 g ( $1 g = 9.8 \text{ m/s}^2$ ) at 13.9 kHz. Fang et al. (2006) was first to demonstrate a MEMS energy harvester using the 31-mode and an end mass, which significantly improved the performance. Their device dissipated 2.2  $\mu$ W into a 21 k $\Omega$  load at a vibration input of 1 g at 609 Hz. The optimized output was 0.3 V in this mode.

The large number of MEMS energy harvesters published since have mostly adopted a similar form similar to that of a cantilever with an end mass with optimizations occurring in fabrication/design or in material properties. An evolution of the simple cantilever design which produced a low frequency and high displacement using an AlN layer was reported by Andosca et al. (2012). Compared to previous designs from the IMEC/Holst Center (such as the one described Elfrink et al. (2009,) who reported  $>30 \mu\text{W}$  excited at 600 Hz), the device reported by Andosca et al. used a silicon beam about four times thinner ( $10 \mu\text{m}$ ) and produced  $128 \mu\text{W}$  for a  $1 \text{ g}$  input at 58 Hz.<sup>49</sup> Sometimes the aim has been to tune the mechanical harvester to a low resonance frequency or to optimize the strain distribution across the beam. This has resulted in designs such as the zig-zag by Karami and Inman (2011) which was reported to reduce the natural frequency of a MEMS beam by an order of magnitude. A comparison of resonantly-driven MEMS devices from literature is presented in Table I.

Table I. Resonant Piezoelectric MEMS Energy Harvesters Reported in the Literature

<i>Reference</i>	<i>Material</i>	<i>Normalized Power</i> $\mu\text{W}/\text{cm}^2 \text{g}^2$	<i>Frequency</i> Hz	<i>Comment</i>
Marzencki (2008) [1]	1 $\mu\text{m}$ AlN	0.22	1495	Dynamic threshold voltage MOSFET diodes used
Muralt (2009) [2]	2 $\mu\text{m}$ PZT	147	870	Interdigitated electrodes
Isarakorn (2011) [3]	0.5 $\mu\text{m}$ PZT	433	2297	MBE-grown epitaxial PZT on STO//Si
Morimoto (2010) [48]	2.8 $\mu\text{m}$ PZT	23	126	PZT transferred from MgO to steel
Hajati (2011) [4]	0.3 $\mu\text{m}$ PZT	$56 \mu\text{W}/\text{cm}^2$	$< 1350$	Broadband design swept with high acceleration ( $\gg 1 \text{ g}$ )
Defosseux (2012) [5]	2.0 $\mu\text{m}$ AlN	354	214	$Q_{\text{tot}} > 580$

Andosca (2012) [49]	1.0 $\mu\text{m}$ AIN	197	58	7.8 mm $\times$ 8.3 mm footprint
Tang (2014) [1]	10 $\mu\text{m}$ PMN-PT	138	408	Lapped PMN-PT single crystal

#### 2.2.4 Non-Linear Mechanical Systems for Energy Harvesting

While linear oscillators are well suited to harvest vibrations very close to their natural frequency, they collect little of the vibration energy existing outside this narrow band. The problem presents when linear systems are used to harvest energy from wide-spectrum vibration sources. Figure 2-8 shows a plot of acceleration versus time captured by an accelerometer on a subject walking on a treadmill by Papatheou and Sims (2012). The vibration frequencies produced by walking were spectrally distributed and were concentrated differently for each of the three walking subjects who participated.

Figure 2-8. Filtered acceleration versus time of a subject walking on a treadmill (left) and the resulting Fourier transform (right) showing the distribution of vibration energy.

Due to the prevalence of wide-spectrum vibrations, energy harvesters utilizing a nonlinear mechanical system have been a recent focus in the literature. Such nonlinear devices allow more of the vibrational energy from natural sources to be utilized.

Nonlinear designs investigated include monostable Duffing, bistable, and frequency up-conversion (typically by impact). Monostable Duffing oscillators have amplitude dependent contributions to the stiffness, which may be either stiffening or softening. This causes the

effective resonance frequency to track the input amplitude. The result for either stiffening or softening systems is a widening of the resonance based on the relative strength of the nonlinearity. Duffing stiffening was used by Hajati et al. (2011) in the form of a MEMS piezoelectric bridge with a central seismic mass.<sup>59</sup> The stretching of the beam imparted a nonlinear stiffness, which resulted in an increasing resonance frequency with increasing acceleration level. Figure 2-9 shows the resonance behavior of the device by Hajati et al.

Figure 2-9. A wide-band MEMS energy harvester using a Duffing stiffening bridge design.<sup>59</sup>

In comparison, a bistable nonlinear system has three unique displacement regimes accessed by increasing acceleration level. This results from a double-well restoring potential which separates two stable states. Intrawell displacement occurs for low forces while relatively high forces result in periodic interwell vibrations. For a range of forces in-between, chaotic vibrations occur between wells. The interwell vibrations are of particular interest for vibration harvesting as steep energy wells with steeply sloped walls can result in high velocity motion of the seismic mass. This snap-through motion substantially increases power per forcing cycle and generates high current. Since it can be triggered by forces of arbitrary frequency, snap-through motion is inherently broad-band.<sup>63</sup> A prominent widely employed bistable design is a piezoelectric on a buckled plate since it produces high velocity through snap motion.' Betts et al.

(2012) modeled buckled laminates and found that a square plate produces the optimal power for a harvester. The repelling force of magnets on the end mass and opposing frame has also been used to study bistable cantilever oscillators and even frequency up converting systems.<sup>67</sup> Karami et al. (2012) designed a nonlinear harvester excited by heartbeats for self-powered pacemakers. Heartbeats are periodic, but their motion contains more than a single harmonic frequency; in response, a linear oscillator undergoes chaotic vibrations. Magnets on the beam and frame created two stable deflection states which the beam chaotically deflected between upon heartbeat excitation; the  $7.3 \text{ cm}^2$  harvester with  $80 \text{ }\mu\text{m}$  of PZT produced  $8 \text{ }\mu\text{W}$ .

Lastly, frequency up conversion has been used to harvest energy from arbitrarily low-frequency force. This method uses an impact or a plucking motion to cause a rigid piezoelectric to ring down and produce a high frequency output. Devices with thinned ceramic PZT wafers effectively use this technique to access high-force low-velocity motion. Pozzi et al. (2012) were able to generate  $2 \text{ mW}$  from a knee joint by plucking ceramic bimorphs rotating inside of a housing. Pillatsch et al. (2013) produced up to  $2 \text{ }\mu\text{W}$  using a piezoelectric bimorph displaced by a rotating magnet.<sup>68</sup>

### **2.3 The Properties of Ferroelectric PZT**

In 1952, Shirane and Suzuki reported a temperature independent phase transition in the lead zirconate – lead titanate solid solution. The tetragonal distortion in lead titanate ( $c/a=1.064$ ) is reduced with the substitution of  $\text{Zr}^{4+}$  for  $\text{Ti}^{4+}$  until a ferroelectric rhombohedral phase

becomes favored. Jaffe et al. (1954) was first to show the increased piezoelectric coefficients near this transition. The improved properties were later confirmed by Berlincourt et al. (1960).<sup>7</sup> The superior piezoelectric coefficients observed by Berlincourt et al. began a worldwide effort to research PZT materials and devices such as: sonars, hydrophones, ultrasound devices, pyroelectric detectors, high voltage transformers, micro-actuators, energy harvesters, and many others.

### *2.3.1 Ferroelectricity in Lead Titanate Systems*

Polar materials are called ferroelectric if the polarization vector can be reoriented between multiple equilibrium states by a realizable electric field. This phenomenon has led to ferroelectric oxides with the perovskite structure ( $ABO_3$  formula) to comprise many technologically important piezoelectric materials. The origin of the ferroelectric distortion (i.e. polarization) in perovskites is discussed by Cohen et al. (1992) to be the result of hybridization between O  $2p$  orbitals and  $d$ -orbitals of the B-cation. Hybridization reduces the B–O repulsive forces (forces which stabilize the cubic non-polar structure); for  $PbTiO_3$  Cohen et al. calculates ionizations of  $Ti^{+2.89}$  and  $O^{-1.63}$  for the distorted Ti–O pair. It was also modeled that  $Pb^{2+}$   $6s$  and O  $2p$  hybridization generate the ferroelastic tetragonal distortion in  $PbTiO_3$ . This distortion favors a  $[001]$  polarization and is accompanied by polarization of the  $Pb^{2+}$  ions. Cryogenic high-pressure XRD and in situ Raman spectroscopy by Ahart et al. (2008) have confirmed that  $[111]$

polarization is favored when the ferroelastic strain of the tetragonal phase is made too energetically expensive. A rhombohedral ground state is observed in  $\text{PbTiO}_3$  above 20 GPa at low temperature (after passing through two intermediate monoclinic phases with [110] polarization on increasing pressure). Tailoring strain chemically can move the [111] polarization minima close to ambient pressure, producing a morphotropic phase boundary in many  $\text{PbTiO}_3$ -based systems (e.g.  $\text{PbZrO}_3$ - $\text{PbTiO}_3$ ,  $\text{Pb}(\text{Mg}_{1/3}\text{Nb}_{2/3})\text{O}_3$ - $\text{PbTiO}_3$ ,  $\text{BiFeO}_3$ - $\text{PbTiO}_3$ ). Anisotropic flattening of the free energy surface occurs near this transition and provides the polarization a low-energy path of rotation along {110} planes. Figure 2-10 compares Gibbs free energy profiles for PZT 60/40 at temperatures near and far from the Curie temperature.

Figure 2-10. Gibbs free energy profiles calculated by Landau-Ginsburg-Devonshire theory. Polarization rotation is favorable between polar phases (T-R), while polarization extension is favorable between a polar and non-polar phase (T-C, R-C).<sup>76</sup>

Destabilizing the polarization orientation in ferroelectrics to achieve high coupling coefficients is known as domain engineering and enabled breakthroughs in high-performance piezoelectric devices. For example, Park and Shrout (1997) reported  $d_{33}$  of 2500 pC/N in <001> poled relaxor  $\text{Pb}(\text{Zn}_{1/3}\text{Nb}_{2/3})\text{O}_3$ -8% $\text{PbTiO}_3$  crystals in the rhombohedral phase near the MPB

and Baek et al. (2011) reported an  $e_{31,f}$  of  $-27 \text{ C/m}^2$  in epitaxial  $\langle 001 \rangle$  PMN–PT domain engineered thin films.<sup>43</sup> For high-power applications where heat generation presents a problem, Mn modification of  $[110]$  poled  $\text{Pb}(\text{In,Nb})\text{O}_3\text{--Pb}(\text{Mg,Nb})\text{O}_3\text{--PbTiO}_3$  has limited the extrinsic contribution to less than 2% to produce  $Q_{33}$  quality factors  $\sim 1000$  with  $k_{33} = 0.90$ . Additionally, large piezoelectric properties have been found near the hexagonal to cubic transition in the  $\text{AlN--ScN}$  system, which has been hypothesized to be due to polarization extension at the polar to non-polar instability.<sup>76</sup>

### 2.3.2 Ferroelectric Domains

Upon the cubic to tetragonal transition, the ferroelectric polarization in a perovskite may develop along any of six  $\langle 100 \rangle_{\text{pc}}$  directions and in the rhombohedral perovskite, along any of eight  $\langle 111 \rangle_{\text{pc}}$  directions, where the subscript pc denotes the pseudocubic cell. Where the polarization is discontinuous, such as the surface, a depolarization field develops. As the material cools further below the Curie temperature ( $T_C$ ) polarization and ferroelastic strain increase; in this case, the energy cost associated with the depolarizing field can be reduced by forming domains. Likewise, the mechanical boundary conditions of the material may cause the ferroelastic distortions to be distributed in various directions to reduce strain energy. Regions of approximately homogeneous polarization are called ferroelectric domains, and the boundaries

where they meet are called domain walls. These boundaries form along low index planes such that they are structurally compatible across the domain wall. These boundaries are generally 1-10 nm wide depending on the angle made. Figure 2-11 shows domain walls found in tetragonal PZT. The final domain pattern in a ferroelectric results from an energy minimization and the domain state is sensitive to external electric fields and stresses as well as to the magnitude of the ferroelastic distortion.

Figure 2-11. Domain walls found tetragonal PZT, 180° wall (left) and 90° wall (right).<sup>8080</sup>

The difference in the thermal expansion coefficients,  $\alpha$ , of the film and substrate has a pronounced effect on the domain configuration. Tuttle et al. (1992) were among the first to demonstrate this using PZT films grown on silicon, sapphire, and MgO substrates. PZT has an  $\alpha$  that is smaller than that of MgO but greater than that of sapphire or silicon. When films were grown on MgO, compressive thermal stress in the PZT film was partially reduced via favoring out-of-plane tetragonal distortions over in-plane polarization. This was observed through an increase in remanent polarization and a shift in XRD intensity from the 200 to the 002 PZT reflection. Conversely, PZT on silicon develops in-plane tensile stress which favors in-plane distortion and polarization. The thermal stress,  $\sigma$ , is also a function the difference between the annealing and Curie temperatures,  $T_a$  and  $T_c$ , and is expressed in terms of  $\alpha$ , and compliances,  $s$ , in

equation 2.12.<sup>45</sup>

(2.12)

When splitting is large enough to resolve  $00l$  and  $l00$  reflections, the effect of thermal stress on domain orientation is readily observed by XRD through the relative intensities of these peaks.

### *2.3.3 Properties of Single Domain Tetragonal PZT*

Single crystal materials are often grown by slowly drawing a seed crystal out from a molten crucible of the material; this method is generally not suitable for PZT since it melts incongruently. Therefore, measurements of single crystal single domain properties are not available for PZT near the morphotropic phase boundary, despite their usefulness for the modeling and benchmarking of textured PZT films and ceramics. Haun et al. collected lattice constant, dielectric constant, piezoelectric coefficient, pyroelectric coefficient, and electrostrictive coefficient measurements across the solid solution using ceramic PZT or sol-gel PZT powders and produced the first complete set of single domain properties for a wide range of PZT compositions.<sup>73</sup> Experimental data were utilized to determine the coefficients in a phenomenological Gibbs energy function that could subsequently be used to describe the PZT phase diagram. The phenomenological constants developed by Haun et al. are widely utilized, including for assessing the properties in oriented films.<sup>42</sup> These  $d_{31}$  data calculated by Haun et al. are used in Chapter 4 to compare the measured  $e_{31,f}$  to the phenomenologically predicted

single-domain values.

#### 2.3.4 *Intrinsic and Extrinsic Contributions to the Properties of PZT*

For ceramic PZT, more than 60% of the piezoelectric effect can arise from *extrinsic* contributions of domain wall and phase boundary motion. In contrast, the *intrinsic* contribution refers to the lattice deformation resulting from the average response of all single domains in the sample (appropriately corrected for orientation). The reduced extrinsic contributions in thin films compared to ceramics arise from greater domain wall pinning. Domain wall pinning results from local electric and/or elastic fields generated by defect complexes, grain boundaries, substrate clamping and other such modifiers of the potential energy landscape for domain walls.<sup>80</sup> This is visualized in Figure 2-12 with a diagram representing a potential surface which a mobile interface encounters (e.g. domain wall) moving among individual (un-correlated) local pinning centers.

Figure 2-12. Representation of local potential energies encountered by mobile domain walls.

Wall motion is irreversible if the domain wall does not return to its initial equilibrium position.

The motion is called reversible if the interface returns to the same position after excursion, while irreversible motion leaves the interface in a new position. The amount of irreversible wall motion

can be assessed using the ac field dependence of the dielectric constant, Equation 2.13 gives the Rayleigh law where the dielectric constant increases linearly with field amplitude  $E_0$ , from its initial value with a slope of  $\alpha$ .<sup>80</sup>

(2.13)

Better quantification and understanding of domain wall pinning contributions from different sources may allow increases in the performance of thin film devices if the domain wall pinning can be reduced by improved processing. The effects of grain size (also grain boundaries), substrate clamping, and residual stress have all been investigated. That work is reviewed here to place the experiments in Chapter 5 in context.<sup>84,85,87,89</sup>

The energy balance between elastic interactions and domain wall formation predicts a parabolic scaling relationship where the domain size is proportional to the square root of the grain size. Cao and Randall (1996) confirmed this for PZT ceramics with grain sizes of 1-10  $\mu\text{m}$ . They observed that smaller grains had fewer domain variants and suggested that this acted in concert with grain boundary pinning to cause low domain wall mobility in fine grain ceramics. It was also shown using Rayleigh law analysis that fine grain BaTiO<sub>3</sub> had lower irreversible domain wall motion than coarse grain ceramics.

The effect of grain size on the contribution to the dielectric constant from irreversible domain wall motion in PNN-PZT thin films was investigated by Griggio and Trolier-McKinstry (2012). An increase in  $\alpha$  from 5.3 cm/kV to 10.6 cm/kV was observed with a grain size increase of 110 nm to 270 nm in 245 nm films, suggesting a considerable increase in domain wall

contributions to the measured dielectric response. This is consistent with previous reports that 90° domain wall motion is suppressed by decrease in grain size of ferroelectric materials.’ Recently the pinning strength of a single grain boundary has been studied using band excitation piezoforce microscopy by Marincel et al. (2014). By spatially mapping the level of irreversible domain wall motion on epitaxial films grown on bi-crystal substrates (a crystal with one grain boundary) they showed pinning strength increases with the angle between grains.<sup>84</sup>

The effect of substrate clamping on irreversible domain motion in PZT films has been investigated through numerous methods involving removing/buffering the film from the stiff substrate. Initial reports of recovered domain wall mobility in PZT films due to mechanical declamping were obtained by patterning films to lateral dimensions close to the film thickness.’ Nagarajan et al. (2002) showed that *a* domains which could not be switched in a 300 nm PZT 20/80 blanket film could be irreversibly switched in a 1  $\mu\text{m}^2$  island; switching was accompanied by a 100% increase in the remanent polarization. Anbusathaiah et al. (2010) used a layer of morphotropic PZT as a locally pliable pseudo-substrate for the deposition of a PZT 20/80 film. The Ti-rich layer was large-grained (perhaps as a result of the underlying layer), the domains in this tetragonal layer were densely structured and mobile under applied field. A third method to characterize a declamped PZT thin film was demonstrated by Griggio et al. (2012); the substrate underneath the film was etched to form a micro-scale thin film diaphragm. When the diaphragm film was cracked, the latent tensile stress in the diaphragm relaxed through curling of the free standing freestanding membranes. This change was accompanied with a 114% increase in  $\alpha$

compared to the unbroken diaphragm. This suggests significant reduction in pinning of irreversible wall motion as stresses are eliminated.<sup>85</sup>

## Chapter 3

### Dependence of Domain State and Film Composition on the Energy Harvesting Figure of Merit

The piezoelectric  $e_{31,f}$  coefficient is largest parallel to the spontaneous polarization in tetragonal  $\text{PbZr}_x\text{Ti}_{1-x}\text{O}_3$  (PZT) films. However, the expected piezoelectric data are typically calculated from phenomenological constants derived from data on ceramic PZT. The dependence of  $e_{31,f}$  on  $c$ -axis texture for {001}PZT thin films was investigated by growing films on  $\text{CaF}_2$ ,  $\text{MgO}$ ,  $\text{SrTiO}_3$ , and  $\text{Si}$  substrates to achieve various levels of  $c$ -axis texture. An approximately linear increase in  $e_{31,f}$  with  $c$ -axis texture was observed for compositions up to 0.43 mol% Zr, 100%  $c$ -domain properties were extrapolated and it was demonstrated that  $c$ -axis PZT films can achieve  $e_{31,f}$  exceeding  $-12 \text{ C/m}^2$  for many tetragonal compositions. The energy harvesting figure of merit,  $e_{31,f}^2/\epsilon_r$  for  $c$ -axis PZT films surpassed  $0.8 \text{ C}^2/\text{m}^4$ . It was also seen that by doping the PZT with 1% Mn caused a 20% increase in the figure of merit by reducing extrinsic contributions to the dielectric constant.

### 3.1 Introduction

Vibrational energy harvesting taps a ubiquitous energy source (mechanical vibrations), and is of interest for powering microelectromechanical (MEMS) sensors and actuators as well as low-power wireless communications.<sup>21</sup> As a result, piezoelectric thin films and devices have been extensively studied for energy generation. Increasing the harvested power level would allow more sophisticated sensor systems, or would enable the duty cycle for data transmission to be increased. Numerous factors are being explored to improve the harvested power levels, including exploitation of nonlinear mechanical systems, improved circuits for energy extraction, and improvements in the piezoelectric material itself. This chapter will concentrate on the latter factor, e.g. how the material can be tailored to MEMS energy harvesting systems. In the case where the majority of the elastic energy is stored in the passive elastic layer, the piezoelectric figure of merit (FoM) for energy harvesting is  $e_{31}^2 f^2 / \epsilon_r$ <sup>55</sup>. All terms in this FoM are functions of  $c$ -domain fraction,  $f_{001}$ .

Lead-based ferroelectrics for MEMS energy harvesters have been reported utilizing a wide range of compositions and crystallographic orientations. Very high FoM are reported for polar-axis oriented tetragonal PZT with compositions near the MPB. Epitaxial (001)PZT (50/50) sputtered on (100)MgO are reported with  $d_{31}$  of  $-100$  pm/V and  $\epsilon_r$  between 200-150; this yielded a FoM between  $0.7-1$  C<sup>2</sup>/m<sup>4</sup>. The largest reported values reported,  $> 1$  C<sup>2</sup>/m<sup>4</sup>, were measured for epitaxial (001)PZT (48/52) and 0.06PMnN-0.94PZT (48/52) sputtered on

(100)MgO.<sup>37,46</sup> The large figure of merit is partly a consequence of the low dielectric susceptibility and high piezoelectric coefficient along the polar-axis in tetragonal (001) PZT. Control of the ferroelectric domain state then becomes one of the key means of tailoring the energy harvesting figure of merit.

Systematic adjustment of  $f_{001}$  was achieved through thermal expansion mismatch between the film and substrate. Substrates with high  $\alpha$  with respect to PZT produce compressive stress in the film, favoring (001) domain texture. In this work, PZT films were grown on CaF<sub>2</sub>, MgO, SrTiO<sub>3</sub>, and Si substrates to demonstrate the achievable values for FoM and to isolate the dependence of  $e_{31,f}$  on  $f_{001}$  and  $x$  individually. An extrapolation was made to estimate  $e_{31,f}$  and the FoM for a single domain PZT thin film.

## 3.2 Experimental Procedure

### 3.2.1 Thin Film Fabrication

PZT samples with Zr concentrations,  $x=[\text{Zr}]/([\text{Zr}]+[\text{Ti}])$ , 0.30-0.63 mol% were grown by chemical solution deposition (CSD) via repeated spin coating at 3000 rpm using 2-methoxyethanol based solutions of 0.4-0.5 molar concentration with 10% excess lead. The solutions were prepared after the method of Budd, Dey, and Payne (1985) using reagents from Sigma-Aldrich. The films were dried and pyrolyzed for 2 min each at 250 °C and 400 °C, respectively, before crystallizing in an RTA (RTP660A, Modular Processing Group) at 650 °C for 1 min with a ramp rate of 3 °C/min; films were deposited on (111)Pt/TiO<sub>2</sub>/SiO<sub>2</sub>/Si,

(100)SrRuO<sub>3</sub>//(100)SrTiO<sub>3</sub> and (100)Pt//(100)MgO substrates. The {100} texture was obtained on Si by depositing a lead titanate buffer layer as described elsewhere.<sup>42</sup> The (100)SrRuO<sub>3</sub> was grown on (100)SrTiO<sub>3</sub> (MTI Corp.) by pulsed laser deposition under conditions described previously. A 120 nm (100)Pt electrode was grown on (100)MgO substrates (MTI Corp.) by RF magnetron sputter deposition (CMS-18, Kurt J. Lesker) using the conditions given in Table II. MgO substrates were annealed for 60 s by RTA at 1000 °C before Pt deposition to remove surface hydration.

Table II. Sputter Conditions for (100) Pt on MgO

Power	Target Diameter	Target to Substrate	Chamber Pressure	Temp.	Deposition Rate	Ar/O <sub>2</sub>
200 W	7.6 cm	12 cm	5 mtorr	750 °C	12 nm/min	90/10

Tetragonal PZT films were also deposited via MOCVD. The ratios of source gas flows were controlled to grow films over a range of compositions; Zr/Ti ratio was measured after growth by calibrated wavelength dispersive XRF (PANalytical PW2404). Three tetragonal compositions were grown at 500 °C  $x = 0.29, 0.37, \text{ and } 0.43$ . Films with  $x = 0.19$  (the highest Curie temperature) were grown at 650 °C to promote  $c$ -domain texture by increasing the compressive stress experienced by the film at the Curie temperature.<sup>82,81,83</sup> Epitaxial PZT films

were deposited on 50 nm (100)SrRuO<sub>3</sub> bottom electrodes deposited by RF sputter deposition in 20% O<sub>2</sub> at 200 mTorr, and at a rate of 0.23 nm/min at 550 °C. Intermediate layers were employed to diffuse the change in lattice parameter between the substrate and the SrRuO<sub>3</sub>. These layers and the substrates for which they were used appear in Table III, which summarizes the PZT films reported on in this chapter.

PZT capacitor structures using Pt top electrodes were patterned by lift-off lithography, for which a detailed account is given in section 5.2.2 (p. 73).. Each capacitor was poled at fields exceeding three times the coercive field for 1 min at room temperature immediately before measuring the piezoelectric coefficient by the wafer flexure method. Average strains less than  $2 \times 10^{-6}$  were measured using surface mounted strain gauges (Omega KFH-1.5-120-D16-11L1M2S). A minimum of three electrodes was characterized per film to obtain an average and standard deviation for  $e_{31,f}$

Table III. Substrates, [Zr] and Thicknesses of (001) PZT Thin Films used to Investigate the

Influence of Domain State on Energy Harvesting Figure of Merit

Substrate:		Electrode:		Film Thickness (nm)			
				[Zr] (mol%)			
PZT Films Grown by MOCVD				0.19	0.29	0.37	0.43
SiO <sub>2</sub> /Si	*(100)SrRuO <sub>3</sub> /LaNiO <sub>3</sub> /Pt/Ti		480	630	1000	460	
(100)SrTiO <sub>3</sub>	(100)SrRuO <sub>3</sub> //		480	630			
(100)MgO	(100)SrRuO <sub>3</sub> //		480				
	(Ba <sub>0.5</sub> Sr <sub>0.5</sub> )TiO <sub>3</sub> //						
(100)CaF <sub>2</sub>	(100)SrRuO <sub>3</sub> //Pt//					460	
	(100)SrRuO <sub>3</sub> //LaNiO <sub>3</sub> //				900		
	(100)SrRuO <sub>3</sub> //Pt//		480	630			
PZT Films Grown by Sol-Gel				[Zr] (mol%)			
				0.30	0.40	0.43	0.48
SiO <sub>2</sub> /Si	(100) LaNiO <sub>3</sub> /HfO <sub>2</sub>				500		
	(100)PbTiO <sub>3</sub> /Pt/Ti						1240
(100)SrTiO <sub>3</sub>	(100)SrRuO <sub>3</sub> //						1220
(100)MgO	(100)Pt//		950	610			100
				[Zr] (mol%)			
				0.52, +1%Mn	0.55	0.58	0.63
(100)MgO	(100)Pt//		860, 920	940	827		720

3.2.2 Characterization by X-ray Diffraction

The crystallographic orientations of the films were characterized using 4-circle X-ray diffraction, XRD, (Philips X-Pert PRO). The  $f_{001}$  was calculated by fitting 200 and 002 peaks using asymmetric Pearson VII functions, asymmetric fits are used to include the intensity from strained regions near domain walls. Figure 4-1 shows two XRD scans along with the peak fits of the films on Si with  $x = 0.19$  and  $x = 0.43$ . The area,  $A$ , under the fitted curves between  $43^\circ$  and  $47^\circ 2\theta$  was used to determine the volume fraction of  $c$ -domains by:  $f_{001} = A_{002} / [A_{002} + A_{200}]$ . The standard deviation,  $\sigma$ , in the intensity at a given  $2\theta$  was calculated as  $\sigma = \sqrt{I}$ . The integrated peak area (and propagated standard deviations in the area) was therefore,  $A \pm \sigma_A$ . Propagation of  $\sigma$  in the calculation of  $f_{001}$  yielded uncertainty limits for  $f_{001}$ . Lattice constants were calculated for the sol-gel deposited film using the Nelson-Riley extrapolation function for  $\theta$ - $2\theta$  scans of the  $\{00n\}$  and  $\{0nn\}$  reflections. The  $d_{n00}$  in-plane spacing was calculated using  $d_{00n}$  and  $d_{0nn}$  and the relationship  $1/d_{(0nn)}^2 = n^2/d_{(n00)}^2 + n^2/d_{(00n)}^2$ .

Figure 3-1. XRD spectra of MOCVD PZT films with  $x=0.19$  (left) and  $x=0.43$  (right). Substrates from top to bottom on left are:  $\text{CaF}_2$ ,  $\text{MgO}$ ,  $\text{SrTiO}_3$ , and Si, on right:  $\text{MgO}$ , Si, and Si (sol-gel

PZT). At 400 °C these substrates have thermal expansion values of 28.4 ppm/K, 13.6 ppm/K, 11.2 ppm/K, and 3.9 ppm/K, respectively. LNO = LaNiO<sub>3</sub>, STO = SrTiO<sub>3</sub>,

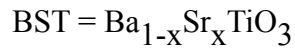


Figure 3-2. XRD scan of PZT 200 & 002 peaks for PZT on Si with  $x = 0.19$  (left) and PZT 400 & 004 peaks for PZT on Si with  $x = 0.43$  (right). The enhanced splitting of the 400 peak was required to assess  $f_{001}$  for the sol-gel film on Si due to the much larger peak width than the MOCVD films, making fits uncertain when 200/002 peaks were employed.

### 3.2.3 Microstructure Comparison by FESEM

Cross sectional FESEM (1530, Leo) images of PZT films on different substrates are shown in Figure 4-3. Fiber textured films grown on Si substrates had columnar grains while epitaxial films on oxide electrodes appeared to be smooth and free of large-angle grain boundaries. Films including (100)Pt electrodes had more grain boundaries than films with only oxide layers, XRD analysis also revealed a weak 110 SrRuO<sub>3</sub> peak for some (100)SrRuO<sub>3</sub>//(100)Pt/(100)MgO substrates. PZT films on all substrates had strong  $00l/h00$  orientation of the perovskite grains; an example XRD is shown in Figure 2 for the films with  $x=0.19$ .

Figure 3-3. MOCVD PZT film cross section selections showing representative microstructure differences between: epitaxial films on single crystals (a-d), fiber-textured PZT on Si (e -f), and films with Pt layers (a-b) compared to oxide-only layers (c-d). The compositions are: a)  $x = 0.19$ , b)  $x = 0.43$ , c)  $x = 0.29$ , d)  $x = 0.37$ , e)  $x = 0.37$ , f)  $x = 0.29$

### 3.3 Results and Discussion

#### 3.3.1 Phase and Domain Content of Films as a Function of [Zr]

The phase makeup of the sol-gel PZT films on MgO was investigated in order to insure that comparisons between the experimental data and phenomenological calculations for tetragonal PZT would be valid. Two distinct lattice parameters were identified for films with  $x = 0.52$ - $0.63$  even though bulk PZT with these compositions is rhombohedral. It is not clear whether the films were tetragonal, distorted rhombohedral, or a mixture of the two. Time dependent phase field modeling by Choudhury et al. (2005a,b) predicts films with  $0.44 < x < 0.58$  will have mixed *c*-axis tetragonal domains with distorted-rhombohedral and orthorhombic phases co-existing. The measured lattice parameters appear to have a discontinuity between  $0.48 < x < 0.52$ . This may be related to introduction of additional phases and would agree with the results of Yokoyama et al. for 2  $\mu\text{m}$  (001)PZT films grown on (100)SrTiO<sub>3</sub> by MOCVD, where a tetragonal-rhombohedral mixed phase region spanning  $x = 0.45$  to  $0.60$  was reported. Therefore, the “tetragonal” region for the growth of PZT films by CVD was considered to extend up to  $0.45 < x < 0.48$ . The lattice parameters calculated from XRD are shown in Figure 3-4 as well as the data showing the 200 family of reflections.

Figure 3-4. PZT lattice parameters determined by four-circle XRD measurements (left) as a function of [Zr] compared to the bulk ceramic (dashed line); bars show 95% confidence limits. XRD scans (right) showing out-of-plane reflections stacked by increasing [Zr], dashed lines are guides to the eye showing the trend in peak position as a function of composition.

The fraction of *c*-axis domain in each tetragonal film was determined from the relative peak areas calculated from the XRD data. Figure 4-5 shows  $f_{001}$  for as well as the propagated error (most fit within the symbol). There were three factors that were found to increase the degree of *c*-domain texture in this set of films: larger substrate thermal expansion coefficients, more Zr-rich compositions (i.e. higher *x*), and increased growth temperature. It is believed that the increase in  $f_{001}$  with increased *x* results from the decrease in transformation strain (tetragonality). This is reportedly a consequence of the fact that cooling between  $T_C$  and room temperature causes a gradual redistribution in domains as a result of the increasing distortion; this effect is reduced with decreased tetragonality.<sup>81</sup>

Figure 3-5. Volume fraction of *c*-domains for {001} PZT films grown on Si, SrTiO<sub>3</sub>, MgO and

CaF<sub>2</sub> (the same symbols are used throughout to denote the substrate). MOCVD films with  $x = 0.19$  were grown at 625 °C while other MOCVD films were grown at 500 °C, a color code is used throughout to denote composition. A dagger (†) indicates weak 110-PZT peaks were present and accounted for in calculating  $f_{001}$ . A double-dagger (‡) denotes samples prepared by sol-gel.

### 3.3.2 Dielectric Constant Analysis

Electrical properties of PZT sol-gel films on substrates of different thermal expansion are shown in Figure 3-6. The temperature dependent thermal expansion coefficients for these substrates are given in Figure 3-7 along with a comparison of the thermal strains which develop in the PZT film on each substrate. The permittivity and piezoelectric coefficient both show a linear dependence on thermal strain in the film. As mentioned in chapter 2, at the Curie temperature the unit cell elongates along [001] and shortens along [100] & [010], as the polarization develops. This, in turn, helps control the domain state. Thermal strain therefore enables a systematic investigation of anisotropy in the dielectric and piezoelectric properties of PZT thin films.

Figure 3-6. Linear change in dielectric constant and  $e_{31,f}$  of poled sol-gel {001}PZT 48/52 films crystallized at 650 °C (950 K) on silicon, SrTiO<sub>3</sub> and MgO substrates as a function of the calculated thermal strain.

Figure 3-7. Thermal expansion coefficient,  $\alpha(T)$ , for PZT and substrates. The colored areas are equal to the thermal strains at  $T_C$  used in Figure 4-6 which are calculated by the integral: .

It is preferable to compare film properties using  $f_{001}$  rather than simply with thermal strain. For this reason  $f_{001}$  was measured for films grown in the tetragonal phase (Figure 3-5). As illustrated in Figure 3-6, at least three stress states were measured for each composition so that a linear regression could be done. The permittivity of PZT capacitors after poling is shown in Figure 3-8; in all cases, the dielectric loss was below 5%. The intrinsic dielectric constant from phenomenology is shown by a straight line.<sup>73</sup> A measured dielectric constant above the intrinsic value was attributed to domain wall motion. It is notable that the experimental values were closest to the intrinsic predictions for films with  $f_{001} > \sim 80\%$ . Poled films with  $f_{001}$  equal to zero or one are expected to have the fewest domain walls.

Figure 3-8. Measured dielectric constants of poled films versus  $f_{001}$ , solid line compares to phenomenological dielectric susceptibility of mixed  $c/a$  domain state. Films match the prediction

exceptionally when  $f_{001} > \sim 80\%$ .

Acceptor Acceptor doping was investigated as an additional path to reduce the permittivity of PZT films. Zhang et al. (2001) reports this effect for films doped with Mn. This was attributed to the observed increase in internal bias field. It was also observed that the field-dependent Rayleigh constant,  $\alpha$ , decreased for Mn-doped films. It is assumed defect dipoles are formed and are pinning sites for domain walls. Epitaxial {001}PZT/Pt/(100)MgO of  $x=0.52$  with 1 mol% Mn had a 15% lower dielectric constant (from 464 to 395); it also increased the internal bias field (Figure 3-9). Poling at 150 °C for one hour further reduced the values to 424 and 343 for the doped and undoped film respectively. This decrease in dielectric constant had no measureable effect on  $e_{31,f}$  and resulted in a 20% increase in the FoM.

Figure 3-9. Dielectric constant versus bias field for epitaxial {001}PZT 52/48 films with and without Mn doping. The lower un-biased permittivity of the Mn-doped films increased the (hot poled) FoM by 20%.

### 3.3.3 Piezoelectric Coefficient Analysis

As a first approximation to describe the  $f_{001}$  dependence of the  $e_{31,f}$  piezoelectric

response, a linear regression analysis confined to pass through the origin was done. Setting the  $y$ -intercept at the origin was justified in the derivation of the piezoelectric coefficient via phenomenology:  $d_{31}=2 \cdot P_r Q_{12} \epsilon_r \epsilon_0$ , where  $P_r=0$  if  $f_{001}=0$ . If the film can be modeled as an ensemble of individually responding domains; then, a linear dependence of  $e_{31,f}$  on  $f_{001}$  is likely. However, in the case where elastic coupling of adjacent domains constrains the piezoelectric responses of well-aligned domains, or inadequate charge delivery prevents alignment of domains through the film thickness, functional properties may increase nonlinearly for  $f_{001}$  near unity. In this condition the linear extrapolation would provide a lower bound for the fully  $c$ -axis textured film. Alternatively, contribution by domain wall motion should be observed to concentrate at medium values of  $f_{001}$ .

The  $e_{31,f}$  for tetragonal films are plotted in Figure 3-10 as a function of  $f_{001}$ . The line of best fit and  $R^2$  value are given on each plot; uncertainty in the extrapolated  $e_{31,f}$  is generated by the 90% confidence interval in the slope. The linear fit accounts for 92% of the variation in  $e_{31,f}$  with  $f_{001}$  and was not impacted by the span of  $f_{001}$  fitted, which ranged from  $\Delta f_{001}=77\%$  ( $21\% \leq f_{001} \leq 98\%$ ) to  $\Delta f_{001}=41\%$  ( $55\% \leq f_{001} \leq 96\%$ ). This suggests intrinsic lattice contributions dominate the direct piezoelectric effect for PZT films for the strain levels in this work ( $\leq 10^{-6}$ ). The line of best fit is within one standard deviation of  $e_{31,f}$  for every sample but PZT on  $\text{SrTiO}_3$

with  $x=0.29$  (dark grey diamond); this set had  $R^2 = 0.77$ . The aforementioned film had lower dielectric constant than a PZT film on  $\text{SrTiO}_3$  with  $x=0.19$ , despite being 13% more  $a$ -axis textured and 10 mol% more Zr-rich. Since the piezoelectric coefficient should scale with dielectric susceptibility, this film may not be of comparable quality. If excluded,  $R^2$  increases to 0.96 for the remaining films with  $x=0.29$ .

From the extrapolations in Figure 3-10, the intrinsic  $c$ -axis  $e_{31,f}$  was predicted for each composition and plotted in Figure 3-11. These are shown alongside the calculations seeded with data from ceramic PZT.<sup>45</sup> The experimental data and model appear to converge as the morphotropic phase boundary is approached: however, it is critical to note that for tetragonal films the experimental  $e_{31,f}$  values are more than twice those from the phenomenological model. Some of this discrepancy may be due to lower compliance in these oriented PZT thin films relative to ceramics.

Figure 3-10.  $e_{31,f}$  versus  $c$ -axis texture for tetragonal PZT films.  $R^2$  for the line of best fit through the origin is given with the value of  $e_{31,f}$  extrapolated to 100%  $c$ -domain orientation.

Vertical bars show one standard deviation in the measured data. Uncertainty in the slope

determines the 90% confidence interval.

Figure 3-11. Experimentally derived intrinsic [001]  $e_{31,f}$  from Figure 4-10 and from phenomenology (dotted line). Measured values of  $a$ -domain {100} PZT films on silicon by Lederman et al. (2001) for comparison.

If the  $d_{31}$  values from Haun et al. are ascribed to these films, an improbably high value of 350 GPa results for the Young's modulus. This suggests the mismatch in the phenomenological and the experimental values are due in part to higher than predicted  $d_{31}$ . It is noted that the  $e_{31,f}$  reported by Lederman et al. (2003) for a {001}PZT 30/70 film on Si (Si promotes  $a$ -domain texture) is 20% higher than the estimated  $c$ -axis value of  $-5.4 \text{ C/m}^2$ . As demonstrated, the largest  $e_{31,f}$  for tetragonal films is not achieved on Si substrates.

### 3.3.4 Figure of Merit Dependence on Domain State

Figure 3-12 shows that FoM in tetragonal PZT films is more sensitive to  $f_{001}$  than to Zr/Ti ratio. Additionally, the FoM for  $c$ -axis PZT films ( $f_{001} > 95\%$ ) was measured as high as 0.8-1.0

$C^2/m^4$ . This is in good agreement with previous measurements of the FoM for individual samples of *c*-axis PZT films. This shows that there is considerable room for improvement of the materials currently used in piezoelectric energy harvesting devices, such as AlN and {001}PZT/Pt/SiO<sub>2</sub>/Si, which have FoM of 0.1  $C^2/m^4$  and 0.2  $C^2/m^4$ , respectively.

Figure 3-12. Average FoM for tetragonal compositions of PZT films. Vertical bars indicate one standard deviation in the calculated value.

### 3.4 Conclusions

Dependence of  $e_{31,f}$  on *c*-axis texture for {001}PZT thin films was investigated by systematically varying  $f_{001}$  using thermal strain. An approximately linear trend in  $e_{31,f}$  was observed for films up to 0.43 mol% Zr, indicating that clamped tetragonal PZT films show little extrinsic contribution in the small signal direct piezoelectric effect. Single-domain properties were extrapolated for PZT and are substantially larger than previous estimates. Also, the FoM for energy harvesting in *c*-axis PZT films achieved values of 0.8-1.0  $C^2/m^4$ . This surpasses the PZT films grown on Si substrates by more than four times and is larger than the FoM of 0.6  $C^2/m^4$

for scandium doped scandium aluminum nitride.<sup>39</sup>

## Chapter 4

### **Fabrication and Characterization of a Low Frequency PZT MEMS Energy Harvester**

This chapter describes efforts to develop processing routes for mechanical energy harvesters that utilize piezoelectric thin films with large energy harvesting figures of merit. Several approaches were considered. First, MgO substrates were etched in hot phosphoric acid to enable transfer of PZT thin films to polymer membranes. Dry etching significantly improved the viability of this transfer, but routine transfer was not achieved here from MgO. Key issues were deterioration of the weak interfacial Parylene bonding and deformation of the membrane resulting from thermal stress. These factors were identified through a series of design changes which targeted various theories investigated different possibilities about device failure such as: size, etch stop material, and exposure to interfaces. One method used was to retain MgO in the device stack, a normalized RMS power of  $8.8 \mu\text{W}/\text{cm}^2 \cdot \text{g}^2$  was calculated from the measured voltage response for a Parylene/PZT/Pt/MgO diaphragm with 2.7 kHz natural frequency. It is predicted that a polyimide membrane should enable a fully released device from MgO. To facilitate low frequency harvesters, a  $1.3 \mu\text{m}$  PZT film was transferred from silicon to a  $2 \text{ cm}^2$  BCB/Parylene membrane (3  $\mu\text{m}$  BCB and 15  $\mu\text{m}$  Parylene) via a  $\text{XeF}_2$  etch. This provided a robust means of releasing the beam with good chemical selectivity. Remaining problems include buckling of the beam due to tension in the BCB from curing on a silicon substrate. The device

was calculated to output as much as RMS  $0.53 \mu\text{W}/\text{cm}^2$  when swept through an arc  $>30^\circ$  displacement and allowed to ring down at 5 Hz. This is the lowest *resonant* frequency reported in literature for a piezoelectric thin film energy harvester.

#### **4.1 Introduction**

In the past fifteen years, many piezoelectric MEMS energy harvesters have been reported in the literature (see Table I). However, only recently have substrates other than silicon (e.g. steel) appeared. The most common device geometry entails use of a thinned segment of the growth substrate as the passive elastic material to make a cantilevered piezoelectric unimorph. Silicon offers numerous methods to process this structure, including the use of SOI (silicon on insulator) substrates. While silicon is widely available and readily micro-machined, it was shown in chapter 3 that superior PZT FoM can be obtained, for example, on MgO substrates. This prompted an investigation into the viability of processing MEMS energy harvesters on MgO.

The fabrication of PZT devices on MgO provides an opportunity to deviate from previous device designs. Given that MgO has neither the strength nor etching versatility of silicon, a different fabrication method may be required. For this reason, transfer of the PZT film from the MgO substrate to a flexible polymer substrate was explored. This had the benefit of providing a reproducible passive layer thickness and a low cantilever resonance frequency with the potential for higher toughness.

Fabrication of devices was done on both silicon and single crystal MgO substrates. The techniques used to deposit and pattern the PZT thin film structures were nearly identical, but the processes used to pattern and etch the substrate differed considerably and are the focal points of

chapter 4. The energy harvesting performance of the devices on Si and MgO is also compared and demonstrates the impact of substrate choice on the FoM.

## 4.2 Process Development and Procedures

### 3.2.1 Thin Film Fabrication

The PZT sol-gel films for this work were deposited in the same way as described in chapter 3. The PZT 52/48 composition was used because this produced the greatest fraction of *c*-domains. A 2 mol% Mn addition on the B site was also employed to reduce domain wall contribution to the dielectric constant. Film thicknesses were typically between 1  $\mu\text{m}$  and 1.6  $\mu\text{m}$ . It was calculated that a polymer  $\geq 14 \mu\text{m}$  in thickness was needed to bring the neutral-axis to the surface of a 1  $\mu\text{m}$  PZT film (assuming 1  $\mu\text{m}$  SiO<sub>2</sub>). For 1  $\mu\text{m}$  PZT grown on MgO, at least 8  $\mu\text{m}$  of polymer was sufficient. Table IV shows the elastic moduli used to determine the amount of polymer required, the heavy black line indicates the desired location in the stack for the neutral axis.,120119 The film-substrate interface and film-polymer interface were critical to successful fabrication. Multiple materials were tested as candidates for these interfaces; the deposition conditions for each material are provided here.

Table IV. Example Neutral-Axis Calculation for PZT/SiO<sub>2</sub> & Polymer Cantilevers

Material	Thickness, $t$ ( $\mu\text{m}$ )	Young's Modulus, $E$ (GPa)	$E_i/E_{PZT}$	Centroid, $y_i$ ( $\mu\text{m}$ )
Polymer	12	2.7	0.031	9.22
Pt	0.1	170	1.16	2.17
PZT	1	101	1.00	1.62
Pt	0.12	170	1.16	1.06

SiO <sub>2</sub>	1	64	1.40	0.5
= 2.22 μm				

Bottom Electrode Deposition:

A (100)Pt bottom electrode on MgO was sputter deposited using the conditions given in Table II. Substrates were annealed at 1000 °C for 1 min before electrode growth. Figure 4-1 shows the relative intensities of the Pt 111 and 200 peaks for electrodes grown on 1 cm by 1 cm (100)MgO substrates at different temperatures and oxygen flow rates. It was found that the Pt 111 peak could be suppressed by increasing the adatom energy. This was done by increasing the substrate temperature to 750°C for sputter deposition. A small amount of oxygen (10% of the gas flow) was also helpful.

Figure 4-1. Relative XRD intensity of Pt on (100)MgO substrates sputtered under a matrix of conditions to increase adatom mobility. Introduction of O<sub>2</sub>(g) reduces 111 peak intensity in favor of Pt 200. Films grown at 750 °C were well textured. Numerous small peaks due to tungsten lines generated by the X-ray source.

Due to the excellent chemical stability (i.e. resistance to etching) of SrRuO<sub>3</sub>, pulsed laser deposition (PLD) was used to grow (100)SrRuO<sub>3</sub> bottom electrodes. A (100)MgO substrate was affixed with silver paste to a heater block, which held the sample at 680 °C for the deposition at a pressure of 160 mTorr in 10% ozone. A 30 min deposition with a laser frequency of 10 Hz from a

polished ceramic target yielded a 250 nm SrRuO<sub>3</sub> electrode.

A sol-gel method based on 2-methoxyethanol (Sigma-Aldrich, 99.9%) was used to deposit (100)LaNiO<sub>3</sub> bottom electrodes on HfO<sub>2</sub>/SiO<sub>2</sub>/Si substrates. Lanthanum (III) nitrate hexahydrate (Aldrich 99.99%) and nickel (II) acetate tetrahydrate (Aldrich 99.998%) were refluxed for 3 h at 110 °C, the 0.2 M solution was spun at 3000 rpm for 30 s and dried at 150 °C and 400 °C for 2 min before crystallizing at 700 °C for 1 min. Six layers produced a thickness of approximately 120 nm. The 30 nm amorphous HfO<sub>2</sub> grown by atomic layer deposition (Cambridge Nanotech Savannah 200 ALD System) using tetra-kis-hafnium and H<sub>2</sub>O at 200 °C for 300 cycles. The 100 nm thermal oxide was grown in a furnace and checked by ellipsometry.

Finally, silicon wafers with Pt bottom electrodes were purchased commercially (NOVA Electronic Materials). These 4" wafers had a 1 μm SiO<sub>2</sub> diffusion barrier beneath the Pt/Ti electrode. A PbTiO<sub>3</sub> orientation layer was used to promote {001} texture on these substrates.

#### Polymer Deposition:

Parylene is the generic term for the modifications of poly-para-xylyene. Parylene C is modified with one chlorine atom and has low permeability to moisture. In a thermal evaporator (Specialty Coating Systems), 10 g of precursor yielded a 14.5 μm thick film. Samples were treated before deposition either by cleaning in oxygen plasma or by A-174 silane to promote adhesion (Specialty Coating Systems). It was observed that parylene Parylene bonded adequately to clean Pt but poorly to clean PZT, the use of a silane adhesion promoter helped marginally. The room temperature deposition onto the sample caused the as-grown Parylene to have much lower

stresses free than the other polymers explored in this thesis.

As an alternative to parylene, bis-benzocyclobutene resin (BCB) was selected. BCB is available in convenient thicknesses and is photo-patternable. The BCB resist (CYCLOTENE 4022, Dow) was mixed with polybutadiene diacrylate (30%?) to impart plasticity and spun on a clean PZT device surface. Drying at 60 °C was followed by an overnight bake at 225 °C in a nitrogen atmosphere. The BCB was flexible with an elastic modulus of 2.9 GPa and a reported residual stress of 28 MPa (on Si). Polyimide was also spin deposited on clean devices yielding films thicker than 10 µm cured at 300 °C.

As a third approach to polymer integration, a dry film resist (MX5015, DuPont) and a polyimide gel pack laminate were applied using a laminating tool. The thicknesses of these materials were 15 µm and 150 µm respectively.

### *3.2.2 PZT Structure Fabrication*

The PZT structures were fabricated from the as-grown film. As the first step, Pt/Ti top electrodes were sputtered onto a lift-off lithography mask. A 20 nm Ti layer between the PZT and the 100 nm Pt electrode increased the interfacial bond strength. A contact aligner (MA6, Karl Suss) was used to align a photoresist etch mask to top electrodes. This was deposited by spinning positive resist, SPR220 or SPR 955 (MicroChem), to a thickness of 8-12 µm. The PZT and bottom electrode were etched by RIE (6500, Tegal).

### 3.2.3 MgO Wet Etching

Since MgO substrates were 0.5 mm in thickness, a wet chemical etch was used (the highest etch rate observed by RIE was  $\sim 1 \mu\text{m}/\text{hour}$  using  $\text{BCl}_3$  gas; this is too slow to practically etch through the substrate thickness). A phosphoric acid solution at  $80^\circ\text{C}$  was reported to yield an etch rate up to  $5 \mu\text{m}/\text{min}$ . The observed etch rate in this work was found to depend on several factors. Stirring the solution to move etch products away from the surface was required or the etch progress stagnated. A phosphoric acid concentration less than 60% wt% in water was preferred in order to maintain a low viscosity for improved circulation. The etch rate is predicted to depend exponentially on temperature but evaporation was problematic above the boiling point of water. It was found that a batch of 50 wt%  $\text{H}_3\text{PO}_4$  stirred at  $85^\circ\text{C}$  produced an etch rate of approximately  $4 \mu\text{m}/\text{min}$ ; the etch rate was very sensitive to the actual temperature. The sidewall angle for the MgO wet etch was close to 30 degrees and was not dependent on etch conditions. Etching of the MgO substrate was a straightforward process. However, device failure resulted from etch damage to the PZT once the electrode/MgO interface was breached. Several device designs were explored in order to understand the vector of acid infiltration to the PZT stack.

#### Cantilever Beams:

PZT cantilevers designed to resonate between 77 Hz and 12 Hz were fabricated on  $1 \text{ cm}^2$  or larger MgO substrates. The resonance frequency,  $f$ , was approximated for devices with  $1 \mu\text{m}$  of PZT using equation 4.1, where  $EI$  is the bending stiffness calculated from the moment of

inertia and the elastic modulus,  $m$  is a concentrated end mass, and  $L$  is the (effective) beam length. As described elsewhere, the effective length was calculated as the beam length plus half the length of the end mass.<sup>49</sup>

(4.1)

Since equation 4.1 assumes a point mass, the accuracy for describing cantilevers with a broadly distributed mass was examined. This is because a distributed mass will impart some force moment on the end of the beam. A finite element (FEA) computation was done for select designs by Dr. Sue Gong (Texas Christian University, Department of Engineering, Fort Worth TX). Table V shows the dimensions of the cantilevers designed for fabrication using 1  $\mu\text{m}$  PZT on 0.5 mm MgO. Equation 4.1 underestimated the natural frequency by 4% or less when the distributed mass was twice the beam length; the frequency was underestimated by 18% when the mass was five times the beam length.

Table V. Dimensions and Natural Frequency for Cantilever Devices on MgO

After PZT deposition, the back of the substrates were polished so the MgO etch in phosphoric acid would proceed uniformly. Substrates with fabricated PZT structures were first coated with 15  $\mu\text{m}$  of Parylene on both sides. The Parylene on the substrate back side was next masked with SPR 955 photoresist. A mask aligner was used to align the back-side etch hole to the front-side devices. Finally, an oxygen and argon plasma was used to etch the Parylene

revealed through the photoresist mask (720, PlasmaTherm). The etch rate was 0.5  $\mu\text{m}/\text{min}$  for 2 min intervals using 200 W in Ar: $\text{O}_2$  flow of 10:80 at mTorr. The MgO was then wet etched from the back side of the substrate by floating the wafer on the surface of the etchant. . The stability of SPR 955 positive resist and JSR 105G negative resist in phosphoric acid was inferior to Parylene, which was the only material investigated found to resist the phosphoric acid solution for several hours. Figure 4-2 shows stages of the cantilever fabrication process flow for a D-type design.

Figure 4-2. Process flow for D-cantilever on MgO transferred to Parylene.

Upon etching through the MgO, the etch solution rapidly attacks the interface between the PZT and Parylene. Furthermore, the adhesion of Parylene to Pt was found to be relatively stronger than the adhesion to PZT, regardless of the use of adhesion promoter. For samples fabricated as in Figure 4-2 the PZT stack detached from the Parylene. For PZT films with Pt bottom electrodes the consequences of this were characterized by wrinkling of the thinned layer and a short circuit condition. The D-cantilever was designed to test that a “vulnerability” of the Parylene/device interface theory regarding to the diffusion of etchant to the Parylene/device interface. Previous designs patterned the PZT and bottom electrode using the same RIE mask, ; this left a Parylene/PZT interface exposed to the etchant. The D cantilever uses separate RIE masks to retain a 60  $\mu\text{m}$  border of bottom Pt encircling the PZT structure. The effect of encasing the PZT beam with a more strongly sealed interface is shown in Figure 4-3.

Figure 4-3. (1) Device backside before complete MgO etch (2) Pt/PZT detaches from Parylene immediately upon exposure, even tearing away from the Pt region which remains flat (3) after all MgO has been etched, Pt/PZT/Pt and Pt/PZT regions have buckled off the Parylene (which remains stretched flat), the Pt boarder also remains flat.

It was shown that release using Parylene on MgO would was not likely be improved by

similar efforts to reduce the “vulnerability” of exposed interfaces. Therefore the “permeability” theory of the bottom electrode was investigated by changing the bottom electrode material. Though Pt does not dissolve in phosphoric acid, it is known that pinholes may exist in the layer. Cantilevers (D) grown on 120 nm (100)Pt/MgO were therefore compared to ones on 250 nm (100)SRO/MgO. In preparation to fabricating a full device, a ~1 mm test membrane was wet released using a 1  $\mu\text{m}$  PZT film on 170 nm SRO/MgO and 15  $\mu\text{m}$  of Parylene. The D-cantilever and test structure, both released with SRO etch stops by hot phosphoric acid, are compared in Figure 4-4.

Figure 4-4. **Upper Row:** (1) Parylene side of 1 $\times$ 1 cm test sample (2) SRO side of test membrane (3) the membrane deforms upward but does not crack (drying rings are seen) **Lower Row:** (4) The back of a fully (MgO) etched D-cantilever shows homogenous fracturing in the PZT beam and the end mass has fallen away (5) SEM of fractured Pt/PZT/SRO beam.

#### Segmented Cantilever Beams:

The unpredicted fracturing of the beam on SRO motivated examination of device designs similar to the successful the test membrane. The next design tests tested a “size” effect; which considers used small features in a partitioned beam. This work was partially motivated by is is similar to the reports of successful transferring transfer of thin ribbons of PZT film to a bulk polymer stamp. Beams were laterally segmented into arrays of 50  $\mu\text{m}$  wide and 100  $\mu\text{m}$  wide strips. These length scales were chosen to be similar to the mean size of the fractured Pt/PZT/SRO film plates previously seen by SEM. These devices were coated in Parylene and released in

a phosphoric acid wet etch. While individual elements did show improved resistance to cracking, the Parylene/Pt interfaces were etched on contact. Rather Once this occurred, the PZT layer than remain on the Parylene they buckled to relax stresses.

Figure 4-5 shows an E-type beam testing intended to test the importance of the a size influenceof the released features. Though these devices appear were somewhat more mechanically robust compared to D-type beams, demonstration is final that an improved interface with Parylene will necessarily beis required for an operative device. This motivated a final design theory to ideally separate the chemical etchant physically from the interface.

Figure 4-5. Pt/PZT/Pt stack fabricated with a single RIE mask to avoid mis-alignment. The large deformation of released segments conclusively shows the Parylene interface can never beshould not exposed to the wet etch.

#### Circular Diaphragms:

In the case of a diaphragm, only the un-patterned blanket bottom electrode is ever exposed to the etching solution. because the top surface and sizes of the device is are totally encased in Parylene. ThisSuch a design emulates the test membrane fabrication, with but uses a larger membrane and top electrode. Two ring electrodes are deposited but the PZT film is not patterned. Parylene deposition of 10  $\mu\text{m}$  is followed by backside alignment and  $\text{Ar}/\text{O}_2$  plasma etching of the Parylene through the SPR 220 mask. The device is then floated on the etchant for the 2-3 hours needed to fully etch the MgO. As an alternative, the type-G diaphragm was fabricated by iteratively stopping and checking the etch to yield a  $\sim 15 \mu\text{m}$  thick MgO

diaphragm. A seismic mass ( 0.1 g Sn-Ag-Cu solder) was super-glued on top of the center-mass for devices to be characterize the energy harvesting performed.

The double electrode configuration separates regions of the diaphragm with opposite curvature. The piezoelectric responses otherwise subtract. Figure 4-6 illustrates separately induced stresses due to bending and to stretching. The radial clamping causes the stretching but also seals etchant from the Parylene. An increase in the natural frequency accompanies the radial clamping as well. Three variants, F, G and H, were designed by changing membrane size and used both either Pt and or SRO bottom electrodes. The sizes were chosen arbitrarily to achieve large and small varieties of device sizes, and of various released widths. Table VI provides the dimensions and film thicknesses used for these samples, and Figure 4-7 gives a process flow for the diaphragms.

Figure 4-6. A diaphragm clamped at the perimeter will necessarily have an inflection point in stress. The top electrodes on the piezoelectric is segmented to avoid cancellation of charges when the membrane is stressed for which the electrode arrangement must be designed. Image from Ref [123]

Table VI. Dimensions of Diaphragm Devices

It was found that neither the range of diaphragm sizes explored nor the etch stop material prevented the parylene interface from being etched. The fully etched released devices at the bottom of Figure 4-7 show the results of the release; the beams on SRO fractured apart and fell flaked off of the parylene Parylene membrane. The destruction of the released diaphragms concluded the final design theory, meant to totally isolate the etchant from the Parylene interface. This indicateddemonstrated that the film deformed upon the wet release from the MgO substrate, and that the bond at the Parylene interface was too weak to prevent the film from deforming beyond the point of failure. This motivated a move away from the high-temperature wet release, and away from MgO substrates for the time. The G device, which was not incompletely released from the MgO, is was electromechanically characterized; the results are given in section 4.3.

Figure 4-7. The process flow for fabricating diaphragms had four steps, Pt/Ti top electroding was followed by 10  $\mu\text{m}$  Parylene deposition. After plasma etching the parylene on the back, the MgO was wet etched. An end mass and contact wires were added after MgO etch.

### 3.2.4 Silicon Dry Etching

The wet etch methods used to fabricate devices on MgO caused critical problems at the Parylene interface. This motivated a switch to releasing PZT structures from silicon. A deep RIE step was tested as a method to expedite the etch process, since the silicon substrates were relatively thick. Etch cycles between 10 min and 0.5 min were selected based on the Si thickness remaining. The chuck was cooled to 0 °C and samples were sub-mounted by taping devices down, as thermal release tape was found to stick to the released membranes. The DRIE etch had a tendency to heat the silicon under the beam, which had a parylene layer. This heat generated large thermal stresses which later warped the freed beams. The DRIE also re-deposited polymer from the Kapton mask onto the Si surface which impeded homogenous etching.

A To ameliorate this, XeF<sub>2</sub> dry etching tool (Xactix) was instead used for the entire Si etch. This process proceeds at room temperature and does not require any sub-mounting or cooling of the sample. Though the XeF<sub>2</sub> etch is isotropic, the selectivity to SiO<sub>2</sub> is excellent. Most importantly, there was no degradation of the parylene/Parylene/PZT interface for this method. The room temperature vapor etch allowed arbitrarily large membranes to be released. As a result, and the device was re-designed to be large (for greater power and lower frequency).

A The beam was designed with trapezoidal tapering was given to the beam to control the curling on release. expression of latent in-plane stress after transfer to a polymer. A beam with a rectangular shape, upon release, attempts to curl both along the beam width and length under the influence of the bi-axial thermal stress. This “cupping” stiffens the beam against deforming along either length or width and the majority of strain is forced to the connection at the cantilever

root (where the cupping is not strong). A trapezoidal beam makes curling along the width less favorable and allows curling along the length to dominate (which stiffens the beam further against curling along the width). Making the beam wider at the root and allowing curling only predominantly along one axis (the length) were critical for distributing the strain energy more uniformly across the length of the beam. Given this, and made a case to employ a full-length electrode was employed to increase the energy harvesting area. (Such full length electrodes would introduce parasitic capacitance for rectangular beams due to non-uniform strain along the beam length).

The process flow to transfer a PZT thin film from silicon by  $\text{XeF}_2$  is given in Figure 4-8. This graph figure flows from top to bottom and shows a cross section taken from the dotted line. The PZT stack was eventually grown on 3" silicon wafers because these were thinner than larger wafers, which expedited the silicon etch. The RIE step stopped on the bare silicon so that nothing would remain under the BCB when the silicon etch was finished. As bottom Pt was exposed during the etch, a region was reserved for the bottom electrode by covering a square in the etch mask with Kapton. BCB was spin deposited next, with Kapton covering the contact pads. After drying the BCB, the Kapton was removed and the BCB was cured. Next, nickel wires were fixed to the sample using silver paste (PELCO Colloidal Silver Paste, Ted Pella); by doing this before Parylene coating, the wires were far less likely to be torn off later. The device was encased in Parylene, which had modest adhesion to the BCB, an adhesion promoter was not used. After coating the device, the backside was polished with SiC paper to remove the Parylene and expose clean silicon only. Finally, Kapton tape was used to mask the backside of the device by hand, defining the trapezoidal etch window, and the device was etched in a  $\text{XeF}_2$  etcher. Etching

through 0.5 mm Si was completed in approximately 600 cycles, each 80 sec in duration. After the release, the beam was liberated from the frame by slicing the parylene Parylene using a razor, and a weight was taped to the beam end. A silicon bar was left under the tip of the beam to serve as a stiff support for adding mass and to prevent width-wise curling of the beam near the tip. This end bar also possessed its own PZT capacitor (with bottom electrode access) intended for integration with rectification electronics.

Figure 4-8. A process flow for energy harvesting devices fabricated from a PZT stack on a silicon substrate. Both surface and cross-section views are given alongside a photo of the device at the particular step.

### *3.2.4 Comparison of Polymer Layers Used*

It was found that there are two critical aspects of transferring a PZT thin film structure from the substrate to a polymer layer. The first is mitigation of thermal stress in the polymer and the second is the development of a strong interfacial bond. Though many factors were evaluated in the release of a PZT film from MgO, all devices failed to develop a sufficient interface strength using Parylene. This same interface was sometimes adequate for devices released from Si by  $\text{XeF}_2$  etching, but if the stress in the PZT structure was high, then delamination from the Parylene was favored to relax this stress. This can be seen in Figure 4-8 for a PZT device deposited with a LNO bottom electrode.

Devices with a polymer membrane of either BCB or polyimide were investigated to solve the interfacial strength problems encountered using Parylene. These layers have similar elastic

modulus and both had excellent bonding to the PZT or Pt surfaces (they could not be pulled off the surface, whereas it was found that Parylene always can be). Polyimide is preferred practically since the BCB resist experiences greater change in viscosity over a period of several days stored at room temperature. The development of the BCB layer allowed devices to be fabricated consistently with excellent mechanical properties. A BCB layer enabled transfer of a PZT film off a silicon substrate using a wet etch in hot acetic acid solution when the PZT was deposited on a 1  $\mu\text{m}$  ZnO sacrificial layer. The high temperature cure shared by these two materials may be the source of the excellent bond strength versus Parylene. However, cooling these materials from a high temperature ( $>200$   $^{\circ}\text{C}$ ) imparts thermal stress.

Tensile stress in the polymers cured at high temperature on silicon is large because the thermal expansion coefficients ( $>30$  ppm/K) are about ten times larger than that of silicon.<sup>109,120</sup> This is problematic for the fabrication of thin flexible membranes; stress in this layer curls the beam such that linear harmonic beam excitation is no longer possible. This is not explicitly problematic, but can prevent the seismic mass from coupling with a  $g$ -vector if the curling is too much. This is demonstrated in the most extreme cases in Figure 4-9 by the beams laminated with the dry film. Using a Parylene (only) layer was also problematic. Some films would peel off the Parylene upon release and curl to relax stress. This is consistent with the deformation upon release seen from MgO devices.

The most successful devices released from silicon were fabricated using only 1-2  $\mu\text{m}$  of BCB, forming a strong bond but avoiding larger tensile stresses. A 15  $\mu\text{m}$  Parylene layer was then deposited over the BCB to move the neutral axis of the device. This second layer was stress free as long as it was not exposed to elevated temperatures.

Figure 4-9. (1) Parylene results in a weak interface, which a: 110 nm Pt-Ti/ 2  $\mu\text{m}$  PZT/ 250 nm LNO/ 100 nm  $\text{SiO}_2$  stack curls away from to relax stress (2) a dry film resist causes the greatest amount of curling and was not viable.

### 4.3 Energy Generation

Two piezoelectric energy harvesting (PEH) devices were compared, one fabricated on an MgO substrate and one fabricated on silicon. After adding seismic masses and affixing lead wires with silver paste, these devices were evaluated using a circuit shown in Figure 4-10. A bench top shaker (F3, Wilcoxon) was used to excite the devices from a 5 V sinusoidal signal given by a function generator (SRS830, Stanford Research Systems). A piezoelectric accelerometer (352C65, PCB Piezotronics) was mounted to the shaker and magnets were then used to hold the device to the accelerometer. The circuit used a resistor bank to enable manual selection of a resistive load for the PEH, the voltage developed on the PEH was read on an oscilloscope. The load which dissipates the maximum power was calculated from the operating frequency,  $f$ , and device capacitance,  $C$ , calculated as  $R_i = 1/(2\pi f C)$ .

Figure 4-10. (1) Schematic of PEH test bed, a device is excited (with a shaker table or by a single impulse) and is connected to an oscilloscope with a 1 M $\Omega$  input impedance, the

device is also connected to a resistive load which is varied to match the device impedance

(2) An accelerometer is placed between the device and the shaker with outputs sent to the oscilloscope.

A  $1.2 \mu\text{m}$  {001}PZT diaphragm was fabricated on (100)Pt/(100)MgO with a dielectric constant of 420 and  $e_{31,f}$  of  $-10 \pm 2 \text{ C/m}^2$ . The device was excited resonantly at 2.74 kHz with 0.39 g acceleration. The open circuit voltage amplitude,  $V_{10}$ , was 57 mV (normalized, 146 mV/g), and the optimum resistance was calculated to be 4.3 k $\Omega$ . The *normalized* maximum in RMS power dissipated was  $8.8 \mu\text{W/cm}^2 \cdot \text{g}^2$ , achieved by dividing the square of the normalized open circuit voltage sensitivity by four times the optimum load:  $(V_{10})^2/4R_i$ . If the signal from this device were to be rectified via diodes, an optimum output voltage ( $\frac{1}{2}V_{10}$ ) of 0.07 V/g would be problematic. This voltage is comparatively low because of the thick MgO annular region underneath the PZT (deliberately left unetched due to the vulnerable parylene interface). This increased the frequency of the mechanical resonance, which has an inverse relationship with the displacement.

A  $1.4 \mu\text{m}$  {001}PZT cantilever beam was fabricated on a commercial platinized silicon substrate with a dielectric constant of 1100 and  $e_{31,f}$  of  $-10 \pm 2 \text{ C/m}^2$ . The beam was also buckled along the width and length due to the combination of residual stresses, this buckling increased the restoring force of the beam for displacements which flatten the cupping of the

beam. The thermal stress in this particular beam was larger than subsequent similar fabrications because a greater amount of BCB was deposited ( $\sim 5 \mu\text{m}$ ). The beam was excited by pulling the end through the unstable region and releasing it, allowing it to ring down at 5 Hz. The exponential time constant,  $\tau$ , of this motion was 3 sec, the relationship  $Q=\tau\omega/2$  provides an estimate of the quality factor,  $Q$ , of 50. The largest open circuit voltage read this way was 0.46 V. Using an optimal load of 21 k $\Omega$  yielded an *absolute* initial RMS power of  $0.53 \mu\text{W}/\text{cm}^2$ . This value is most accurate to give in absolute power, rather than in sensitivity. This is because the cupping of the buckled beam caused the voltage sensitivity with acceleration to differ from linear behavior. A steady state (forced) excitation of the device at 0.01 g produced a 90 mV signal ( $23 \text{nW}/\text{cm}^2$ ). The output voltage is larger in this device than for the diaphragm due to the large deflections (millimeters) which accompany the lower frequency; however, the piezoelectric voltage coefficient is lower compared to the device on MgO, which had a relative permittivity of 420.

#### **4.4 Conclusions**

This chapter provides an account of details the specific materials and methods appropriate for transferring PZT thin films onto flexible polymer membranes. Films deposited on MgO substrates had superior figure or merit for energy harvesting compared to PZT films deposited on silicon. Additionally, etching MgO substrates was easily done in a hot phosphoric acid solution using a parylene mask. Unfortunately this mixture also etches PZT. No conditions were found for which parylene protected the PZT layer at the end of the etch. Dry etching significantly

improved the viability of the transfer, but was not possible on MgO. The key issues for the transfer of a large-area PZT film to a thin, flexible, polymer membrane were deterioration of the interfacial bonding) and deformation of the membrane resulting from large thermal stress. Interfacial strength was improved using spinnable polymers with high cure temperature (BCB and polyimide), while beam curling was reduced via room temperature deposited polymer (Parylene).

A normalized RMS power of  $8.8 \mu\text{W}/\text{cm}^2 \cdot \text{g}^2$  was calculated from the measured voltage response for a diaphragm with a 2.7 kHz natural frequency, which was not fully released from an MgO substrate. It is anticipated that using a polyimide membrane rather than Parylene may enable a fully released device, which would result in greater power. Additionally, a PZT thin film of  $2 \text{ cm}^2$  was transferred from silicon to a BCB/Parylene membrane via a  $\text{XeF}_2$  etch. This beam was cupped upward due to tension in the BCB from curing on a silicon substrate. The device was calculated to output as much as RMS  $0.53 \mu\text{W}/\text{cm}^2$ .

Similar devices, such as a  $1 \mu\text{m}$  PZT thin film transferred to  $18 \mu\text{m}$  polyimide by Park et al. also curled upward; they reported 1 nW power transferred for a 115 Hz 1 g excitation. The AlN devices reported by Andosca et al. output  $128 \mu\text{W}$  at 58 Hz for a 1 g excitation. , This thesis reports the first but thus far there is not a MEMS piezoelectric resonant energy harvester reported to that operate resonates at 5 Hz.<sup>49</sup>

## Chapter 5

### Mobility of Domain Walls in Released PZT Thin Films

Through Rayleigh coefficient analysis, the impact of mechanical declamping on the dielectric response of {001} PZT thin film membranes was compared to more generally the impact of reduced elastic restoring force. This was done both by comparing PZT samples in which the substrate was undercut using a  $\text{XeF}_2$  release process, and to samples in which buried electrodes with PZT buffer layers were used to partially “free” a PZT layer from the underlying substrate. Allowing in-plane stress to partially relax for aAlt was found that when a 1.17  $\mu\text{m}$  thick PZT film, was releasedd from the substrate as a 300  $\mu\text{m}$  circular “tab”, the irreversible Rayleigh constant  $\alpha$  increased by 37%. Also, tThe degree of relaxing stress greweffectincrease in domain wall mobility on release increasedwas more notable with larger PZT film thicknesses; similarly releasing a 1.64  $\mu\text{m}$  PZT film increased  $\alpha$  by 72%. The lateral dimension of the membraneIn addition, it was found that residual tensile stresses in the film also controlled access to reduced irreversible wall motion. Making elements smallerThe elastic restoring forces on the membrane were reduced by fracturing the membrane into progressively more sections. This increased  $\alpha$  up to 125 cm/kV for a diaphragm sectioned into quarters. In contast, lLocal substrate release without removing the residual tensile stresses in the diaphragm was found to have little effect on domain wall motion. other than modifying frequency dispersion for measurements at 200 kHz. The remaeneant polarization was not strongly dependeant on either the film thickness or the mechanical clamping conditions. Declamping from size/dimensional effects is apparently more

effective at removing 90° domain walls than declamping a 100's  $\mu\text{m}$  lateral polycrystalline film from rigid clamping. Decreasing 90° domain back-switching in *clamped* films with decreasing tetragonality may reconcile back-switching after release for PZT 30/70 films while no  $P_r$  increase results for PZT MPB films. A MEMS bridge was used to measure the piezoelectric coefficient for a partially relaxed released thin film by using a wafer flexure method using with an electrode configuration which enable the charge and the strain to be measured separately dual-purpose electrode with piezoresistive sensitivity. Field The field dependence of  $e_{31,f}$  was in good agreement with the field dependence of  $P_r$

## 5.1 Introduction

The comparatively low levels of ferroelastic domain wall motion in thin films, as compared to bulk ceramics of the same composition, is problematic not only due to reduced extrinsic contributions to the dielectric and piezoelectric properties, but also because it limits the ability to reorientation of non-180° domain walls during poling. As demonstrated in chapter 3, the strong dependence of the room temperature domain configuration on the substrate CTE may cripple certain energy harvesting figure of merit functional properties if the domains are not able to be reoriented upon poling. Possible reasons for the significantly lower extrinsic contributions in PZT thin films compared to bulk were mentioned in chapter 2. Of these contributing sources, clamping from the substrate has recently become a focus in the literature and has been reported to be particularly deleterious. Declamping has been demonstrated by patterning of meso-scale structures and by undercutting of thin films.<sup>89,92</sup> This chapter builds on the previous work by quantifying the changes in reversible and irreversible domain wall motion which are specific to well-defined declamping conditions.

To separate the influences of “local” and “global” declamping on extrinsic contributions, several PZT device variants were conceived and investigated, as shown in Fig. XXXXXX. A 300 μm diameter circular *membrane* (released film), attached to the substrate as a “tab” (which will subsequently be referred to as the released film), was compared to one bound around the perimeter. Because the released film allowed the one membrane to deform out of plane, the influence of the global stress on the domain mobility from global stress is could be

isolated from that of local stress release. In this context, local stress release refers to the case where the case where the membrane can distort locally, but the average tensile stresses holding the diaphragm taut are essentially unchanged from the stresses in the clamped film. These devices designed to release local stresses could also be fracture in order to relieve the global stresses as well. was also released such that it could be subdivided.

A In addition, a “bridge” variant was also investigated designed to enable measurements of the piezoelectric coefficients of released films. A schematic of the device, including the electrode scheme is shown in Fig. YYYYYY. Previously, measurements of the remanent piezoelectric coefficients of bridge structures were complicated by inadequate knowledge of the applied strain states. To circumvent this difficulty, the top electrode was patterned into a strain gauge on the bridge. Depending on the electrical connections, this could be used either to measure the charge or the strain. The intent of fabricating these devices was to determine if irreversible non-180° domain wall motion would result in increased  $e_{31f}$  for globally released PZT membranes.

In addition to undercuttingFinally the silicon substrate from PZT films, a thin film bi-layer was fabricated via depositing a 30 nm Pt electrode between two PZT films. It had been shown that a PZT 30/70 film grown directly on PZT 52/48 possessed a more complex and mobile domain configuration than a film deposited directly on the bottom electrode., indicating This was attributed to mechanical de-pinning of the top piezoelectric layer.<sup>94</sup> If the release of local interfacial pinning also increases irreversible domain motion, then such a bi-layer structure may exhibit higher domain wall mobility.

## 5.2 Experimental Procedure

### 5.2.1 Thin Film Deposition

Three {001} PZT 52/48 thin film structures were deposited by the sol-gel method. In each case, Si wafers (NOVA Electronic Materials) with a 100 nm thick thermal SiO<sub>2</sub> thermal oxide were used as the substrates. 30 nm of Ti (CMS-18, Kurt J. Lesker) was deposited at a pressure of 2 mTorr. This was oxidized to a 60 nm (111) of TiO<sub>2</sub> layer was then grown by sputtering 30 nm of Ti metal (CMS-18, Kurt J. Lesker) at a pressure of 2 mTorr then annealing the titanium in with flowing oxygen in an RTA for 15 min at 700 °C. The 110 nm Pt bottom electrode was sputtered at 600 °C at a base pressure of 8 mTorr.

As described elsewhere, {001} perovskite orientation was developed nucleated using with a seed layer prepared using a 0.15 M sol-gel solution of Pb<sub>1.4</sub>TiO<sub>3.4</sub> spun at 1500 rpm for 45 s. The wafer was pyrolyzed and placed on hotplates at 250 °C and 375 °C for 2 min each, . this This layer was annealed crystallized for 1 min at 550°C using a 3°C/sec ramp rate.<sup>42</sup> The substrates were then coated with 0.45 M PZT (115/52/48) solution to which 7 vol% acetic acid was added 15 min before spinning. The pyrolysis was conducted using the same conditions described above, but with an annealing step at 700°C. The annealed thickness of each PZT layer was approximately 110 nm. PZT layer deposition was repeated until three film thicknesses were obtained: 1640 nm, 1170, nm, and a bi-layer film of 1040nm and 600 nm separated by 30 nm of Pt (which had been sputtered at room temperature).

Figure 5-1. XRD for the {001} textured PZT films: a 30 nm Pt electrode between layers of PZT had only minimal impact on the degree of {001} texture. The single layer film is 1.17  $\mu\text{m}$  thick, the 1.64  $\mu\text{m}$  film was obtained by depositing an additional 5 layers on a portion of that substrate.

The PZT films had predominately (001)-texture as characterized by XRD (X-Pert Prop MPD, PANalytical). Figure 5-1 shows the XRD spectra patterns of PZT films with and without the buried Pt electrode. The films were also characterized by FESEM (1530, Leo) to insure that all samples were free of cracking and surface pyrochlore. Figure 5-2 shows the surface and cross-section FESEM. A profilometer was used to measure the film thicknesses (P-16, Tencor). Single layer PZT films were 1.17  $\mu\text{m}$  and 1.64  $\mu\text{m}$  thick respectively. The bi-layer PZT film was 1.04  $\mu\text{m}$  thick above the buried electrode and 0.60  $\mu\text{m}$  below

Figure 5-2. FESEM showing surface and cross-section for three PZT structures investigated. Thicknesses were 1.17  $\mu\text{m}$  and 1.64  $\mu\text{m}$  (a. and b., respectively); the bi-layer PZT film (c.) was 1.04  $\mu\text{m}$  above the buried electrode and 0.60  $\mu\text{m}$  below. The black line segments denote 0.5  $\mu\text{m}$ .

XRD of the bi-layer film shows that the buried Pt electrode only slightly degraded the texture of the subsequently deposited PZT. Lead titanate orienting layers have been used in

{001} oriented multi-layer PZT films by Sanchez et al. to retain good texture after four buried Pt layers. In this case, the slow ramp rate during annealing was sufficient to achieve good {001} orientation in the second PZT layer, similar to the single layer PZT films. As an estimate of the texture fraction, the Lotgering factor was calculated to be ??????. FESEM revealed some porosity between sol-gel layers for all films, shown most strongly in the bi-layer structure of Figure 5-2c. This film also had larger grains and a grain substructure, indicated by jagged grain boundaries and rough topology. This unique grain size is presumably a result of the buried electrode since the solution aging and processing conditions were identical for the three samples.

### 5.2.2 Test Structure Fabrication

Three device geometries were employed to characterize the de-clamped PZT membranes. Circular membranes with 300  $\mu\text{m}$  diameter electrodes were released in two geometries. One was separated from the surrounding film by a 15  $\mu\text{m}$  wide etch trench; this allowed the membrane to deform under latent stresses in the stack (relaxing some global stress). An identical circular membrane was centered between eight 30  $\mu\text{m}$  diameter etch holes; this released the interfacial clamping from the substrate without allowing the membrane to relax any global stress. The bridge membrane was 0.46 mm wide with 1.5 mm between clamped sides, an aspect ratio of 3.2. A serpentine electrode with twenty-five 10  $\mu\text{m}$  wide traces, aligned along the beam length, was deposited in the central third (0.5 mm) of the bridge forming a uniaxial thin film strain gauge with gauge factor of  $\sim 6.2 \times 10^6$ . It was assumed the strain perpendicular to the bridge could be estimated using the Poisson's ratio of PZT, this was checked against a measured value from an identical strain gauge aligned perpendicular to a bridge. These test structures were

fabricated in parallel by the following procedure.

#### Lift-off Lithography:

The devices were patterned using a double layer resist using LOR-2A and SPR3012 (Shipley Megaposit, Dow). LOR-2A was spun at 4000 rpm for 45 s and baked at 185 °C for 2 min. SPR 3012 was spun using the same conditions and baked at 105 °C for 1 min. A contact aligner (MA6, Karl Suss) exposed the resist in hard contact with the mask at the energy of 7 J/cm<sup>2</sup>. The 1 μm thick PZT substrates stacks required a 5 sec exposure; the 1.6 μm PZT substrate required a 6.5 sec exposure, presumably due to increased absorption of I-line radiation by the PZT. A 1 min rinse in CD-26 (Microposit MF, Dow) developed the features. Underexposure by 0.5 sec or more caused the finest features not to develop. Overexposure by 1 sec or more caused excessive undercutting which destroyed the 3012/LOR reentrant structure for the finest features.

After develop, cleaning in oxygen and helium (3:1) plasma for 1 min at 200 W was done to de-scum the PZT surface (M4L, MetroLine). Top Pt electrodes were sputtered at room temperature before lifting off the resist in acetone then CD-26, the samples were then annealed at 650 °C for 10 min. Figure 5-3 shows the electrode lithography features in orange.

#### Reactive Ion Etch:

An etch mask was patterned using KMPR 1010 negative resist (MicroChem) spun on at 2000 rpm for 45 sec for a target thickness of 10 μm. The surface was pre-coated with LOR-2A spun at 5000 rpm for 40 sec and baked at 185 °C; this was required to prevent KMPR from permanently bonding to the Pt features on the surface. The etch mask was aligned to the top

electrodes and exposed for 60 sec. A 2 min post exposure bake at 105 °C was followed by an 8 min develop in CD-26. Figure 5-3 shows the RIE lithography features (ultimately to be the etch pits) in blue.

The samples were sub-mounted to a Si carrier wafer using thermal release tape (REVALPHA, Nitto Denko Corp.) so they could be etched in an ICP-RIE (NE-550, ULVAC).

Table VI contains the etch parameters used to pattern the PZT structures.

Table VI. ICP Etch Conditions for PZT and Pt

Material Etched	Flow Cl <sub>2</sub> sccm	Flow Ar sccm	ICP Power Watts	Chuck Power Watts	Pressure Torr	Time sec
PZT	25	0	900	90	12.0	30
Pt	30	40	700	50	10.0	60

Once the Si substrate was exposed, samples were removed from the carrier and the etch mask was stripped in 70 °C Remover-PG (MicroChem) for one hour. The samples were then annealed on a hotplate at 500 °C for 1 h to drive off hydrogen and reduce any crystallographic damage caused by the etch. Fences of re-deposited material and/or resist were left around the etched holes but did not impact the function of the device. It is reported that etching Pt with a high density plasma at low pressure (<10 Torr) reduced fencing. Figure 5-3 shows etch holes which did, and did not, retain fences.

#### XeF<sub>2</sub> Silicon Etch:

The RIE features were used as access areas to undercut the Si substrate. XeF<sub>2</sub> etches Si,

Mo, and Ge with excellent selectivity between  $\text{SiO}_2$  and Si. This allows superb undercutting, even through small holes. A  $\text{XeF}_2$  etch tool (Xactix) was used to undercut the PZT structures. Between 300 and 30 etch/purge cycles were done to undercut features by different amounts. Intermittently, the etch progress was checked by fracturing a feature to observe the undercut. This was the most pragmatic method as the etch rate is determined by the moles of Si removed and is therefore highly non-linear as the etch pits evolve in shape. One etch cycle lasted 1 min.

Figure 5-3. **Upper Row:** (1) Mask design for locally released, “tab” membrane (2) Released “flat” membrane, no substrate clamping and no deformation (3) Material was sometimes seen redeposited on resist walls (4) Membrane A membrane cleared away was fractured to revealing reveal the silicon etch pits. **Middle Row:** (1) Mask design for globally released (relaxed) membrane (2) Released ‘tabs’ relaxed downward and free to deformed freely when probed excited (3) Cracking of the undercut film was observed concentrated in locations where the etch pits showed tight curvatures. **Lower Row:** (1) Mask design for relaxed bridge with uniaxial strain gauge (2) The uniaxially released bridges curl along the width to relax stress, and are contacted on pads at both sides

The PZT structures deformed upon release from the bulk substrate. This resulted in a downward curl of the structures due to the relative thermal stresses of the SiO<sub>2</sub>, PZT and Pt layers. The Pt cools into greater tension than the PZT due to the larger thermal expansion coefficient. The SiO<sub>2</sub> layer is apparently too thin (100 nm) to cause upward curvature of the released PZT structure. Figure 5-3 shows FESEM images of the three released structure variants next to the (overlaid) mask features used to pattern them.

### 5.2.3 Electrical Characterization

Polarization-electric field loops were collected on a Precision Multiferroic tester (Radiant Technologies) at a period of 10 ms; the first loop was automatically discarded by the software. The dielectric constant and loss were measured on an impedance analyzer (HP4248, Hewlett Packard). De-aging of the electrode was done by sweeping the AC amplitude from the  $V_C$  down to zero. Poled Rayleigh measurements were done by holding above the coercive voltage for 20 sec before beginning the measurement.

The piezoelectric constant was measured by the wafer flexure method, as shown in Figure 5-4. A pneumatic force bends the sample at 4 Hz via a Si carrier wafer. Microprobes were used to contact the electrodes to measure piezoelectric current and 100 nm Pt thin film strain gauges contacted on opposite sides of the PZT bridge. This was used to measure the average applied uniaxial strain. The serpentine electrodes were also the charge collecting electrodes; the and the voltages were measured across the top and bottom electrode on using a lock-in amplifier (SRS830, Stanford Research Systems). Strain was calculated by with equation 5.1, where  $GF$  is the gauge factor of Pt ( $\sim 6.2$ ),  $\epsilon$  is strain, and  $V_{out}$  and  $V_{DC}$  are the sensed and the supplied voltages respectively,  $V_{DC} = 4$  V.

(5.1)

Figure 5-4. Wafer flexure method setup for strain and piezoelectric charge measurement. A pressure chuck flexes a carrier holding the sample. Probes connect to a strain measuring circuit (red) and a charge measuring circuit (green).

## 5.3 Results and Discussion

### 5.3.1 Polarization

The remanent polarization directly shows quantifies the relative changes in irreversible mobility of the changes in domain state though the degree of permanent reorientation of domains under as a function of a field excursion. For tetragonal PZT 52/48,  $P_S$  is  $48 \mu\text{C}/\text{cm}^2$ ; this enables an  $f_{001}$  estimate in via the ratio  $P_r/P_S$ , though  $P_r$  are also directly comparable as the films are chemically identical.<sup>73</sup> Primarily of particular interest was whether, a comparison of clamped and released films can show, via increased would show a difference in  $P_r$  if due to changes in the pinning strength for of  $90^\circ$  domain walls has decreased. Comparisons are made to For example, Nagarajan et al., who showed that patterning a PZT 20/80 film into a  $1 \mu\text{m}^2$  island increased  $P_r$  if the film was sufficiently thick to have  $90^\circ$  domains ( $>100 \text{ nm}$ ).<sup>93</sup> Islanded films relax global stress while keeping the interface locally clamped. ; In this work ads new  $P_r$  data for the two remaining different stress states: globally & locally relaxed (named “global”), and globally clamped but locally free (named “local”). The field dependence of  $P_r$  for virgin devices is shown in Figure 5-5. The three release conditions (global, local and a clamped continuous film) are shown for the three film thicknesses. Field dependant dependent  $P_r$  of the locally released device is given to the mechanical limit until cracking of the devices was observed. It was found that the, field dependant dependence of  $P_r$  of the clamped device was

different between virgin and poled states, hence, these data are and is given for increasing and decreasing field.

The  $P_r$  reveal that virtually no de-pinning results from local release at the substrate interface. That is, the evolution of the hysteresis loops is essentially unchanged for fully clamped films and for those that have been undercut, but still experience the global stress states that hold the diaphragms taut. In contrast, the Comparing to globally released devices that it is clear that relaxing in-plane stress and allowing the film to deform is responsible for the large decrease in pinning strength of domain walls develop larger remanent polarizations for smaller field excursions, which leads to the relative increase in  $P_r$  for fields (below 300 kV/cm).

It is interesting that there is virtually no difference in the maximum remanent polarizations Field de-aging has occurred by (e.g. for fields  $\sim 500$  kV/cm) for in the clamped devices and  $P_r$  becomes equal (or greater) to that for the and globally released film devices. This clearly differs from reports on island films. The de-aging onset field shows thickness at which the large increase in remanent polarization dependence occurs increasing from 226 kV/cm to 358 kV/cm with a 30% reduction in film thickness. The  $P_r$  from of clamped films (measured backwards on decreasing field excursions, after exposure to ac fields of from 625 kV/cm) demonstrates hysteresis due to this field de-aging. This can be shown Devices could also be alternatively by thermally de-aging the devices in a box furnace at by treatment in a box furnace at 400 °C for 40 min (10 °C/min ramp); Figure 5-5 shows  $P_r$  of clamped and released devices measured within 24 hours of thermal de-aging clamped and released devices.

Interestingly, annealing the globally free membrane did not change the degree to which maximum  $P_r$  could be increased relative to  $P_S$ . Comparing these devices to PZT thin film islands aids the interpretation of these results.

Figure 5-5.  $P_r$  is compared for three release states: global & local, local only, and clamped.

Globally released devices show an early increase in  $P_r$  for modest driving fields; clamped devices required larger fields to de-pin walls, but achieve equal or greater comparable  $P_r$ .

Annealing devices above  $T_C$  facilitated the increase in  $P_r$  by depinning the aged films.

Modest domain pinning remained in both clamped and free thin films; seen via the ratio of  $P_r/P_S$ , which was between 63%-72% for a maximum field of 625 kV/cm. This indicates either that a majority of the  $c$ -domains have become aligned, or that the films may be locally rhombohedral, though an accurate  $f_{001}$  is not wisely estimated without a comparison to XRD analysis. The One possibility for the much larger increase in  $P_r$  increase observed in reported for tetragonal PZT island structures (versus continuous films) provides good agreement that ability to is that reduce the restoring force for the domain wall structure associated with the residual stresses restoring force, not the interfacial clamping per se, primarily that affects the degree of irreversible switching.<sup>94</sup> In fact, Nagarajan et al. reported that islands larger than  $10 \mu\text{m}^2$  were

essentially clamped by a thick Si substrate. The smallest devices in this work were 300  $\mu\text{m}$  diameter disk membranes; it is possible that a strong self-clamping effect remained due to the stiffening geometry of the released device.

Alternatively, it is possible that the discrepancy between this work and the work of Nagarajan is associated with a difference in the composition or microstructure of the PZT films. Consideration should be given as well to the low tetragonality of the MPB PZT used in this work. Investigation by synchrotron XRD of  $90^\circ$  domain switching in  $\{001\}$  PZT 30/70 films prepared in a similar way to the MPB films discussed here, and that were, released by  $\text{XeF}_2$  substrate undercutting, reveals reduced back-switching (versus clamped films) upon poling for 2 min at 190 kV/cm. For a 1.9  $\mu\text{m}$  film with  $f_{001} = 24\%$  (as-grown), global release resulted in four times more permanent reorientation relative to a clamped area of the film ( $\Delta f_{001}$  of 16% versus 3.8%). The high tetragonality of this composition has the effect of decreasing the fraction of  $c$ -domains in the as-grown film as well as increasing the pinning of the domain wall due to the larger strain associated with reorientation. The disparity in tetragonality and in  $f_{001}$  may be the source of the differences seen between clamped and free devices for these different studies of  $\text{XeF}_2$  released PZT membranes. Tetragonality and elastic restoring force are should be reflected in the potential-well depth for the domain structure, but the strength or coupling of these factors has not been described in this work. A larger matrix of samples would demonstrate explicitly the evolution in  $90^\circ$  domain backs-witching between tetragonal and MPB PZT films (specifically, between clamped and relaxed films).

### 5.3.2 Rayleigh Law Behavior

The Rayleigh law from equation 2.13 was used to compare the amounts of reversible and irreversible domain wall motion for the various states of substrate release. The  $\epsilon_{\text{init}}$  term contains those polarization sources which act reversibly, i.e. lattice distortion and those domain walls which return to their initial positions. The  $\alpha$  term shows the rate at which the polarization permittivity contribution is acquired increases as the driving field to escape (local) potential wells increases. This term relates to the irreversible motion of domain walls which have travelled over barriers in the potential surface. Figure 5-6 shows these parameters measured for nine structures (three release states for three thicknesses), the films were de-aged first with a decreasing amplitude AC field and a linear fit was made to the region of 6-9 kV/cm.

As was observed from the PE loops, the effect of only locally declamping produces the film is mostly negligible changes in the Rayleigh behavior. In fact, the only observed difference was in  $\alpha$  at frequencies above 200 kHz. Clamped films maintained a constant frequency coefficient but a roll-off occurred in locally released membranes as some domains relaxed out of the response. This is also observed in the globally released films and implies a decrease in the elastic restoring force for domain walls. The logarithmic frequency coefficients for  $\epsilon_{\text{init}}$  and  $\alpha$  are given in Table VII. The frequency coefficients show that local release has little effect on the magnitude of domain wall motion.

Figure 5-6. The Rayleigh parameters  $\epsilon_{\text{init}}$  and  $\alpha$  are shown for different release conditions. Local declamping has little effect on the Rayleigh response, but global declamping universally leads to a smaller irreversible response and nearly doubled (for thicker layers) the irreversible contribution.

Griggio et al. has also reported frequency coefficients for Rayleigh parameters and found that clamped films generally had lower  $\alpha$ ,  $\sim 12$  kV/cm, but that  $\alpha$  could increase to  $\sim 21$  kV/cm when locally released. This work shows  $\alpha$  20-40 kV/cm was more typical for clamped and locally released films alike (strongly dependant dependent on thickness). It is possible that some of these differences arise from use of different field ranges for determination of the Rayleigh response. In this work, the effect of global declamping was an increase in  $\alpha$  up to 72 kV/cm and a decrease up to 9% in  $\epsilon_{\text{init}}$  (for a 1.64  $\mu\text{m}$  film). Increase The increase in  $\alpha$  shows that domain walls are pinned less strongly on average and therefore move irreversibly between wells under lower applied fields. This is consistent with the increase in  $P_r$  for globally released films.

Table VII. Rayleigh Frequency Coefficients for 300  $\mu\text{m}$ . The equations describe the frequency dependence for frequency in Hz, kHz???

$\epsilon_{\text{init}} = A - B \ln(f)$	clamped	local release	global release
1.17 $\mu\text{m}$ PZT	1239 – 22.8 $\ln(f)$	1198 – 21.3 $\ln(f)$	1177 – 25.9 $\ln(f)$
1.04 $\mu\text{m}$ bi-layer PZT	1451 – 26.6 $\ln(f)$	1482 – 30.5 $\ln(f)$	1446 – 34.0 $\ln(f)$
1.64 $\mu\text{m}$ PZT	1580 – 32.6 $\ln(f)$	1580 – 32.6 $\ln(f)$	1432 – 34.8 $\ln(f)$
$\alpha = A - B \ln(f)$	clamped	local release	global release

1.17 $\mu\text{m}$ PZT	$31.6 - 0.802 \ln(f)$	$30.1 - 0.869 \ln(f)$	$43.2 - 1.42 \ln(f)$
1.04 $\mu\text{m}$ bi-layer PZT	$45.7 - 1.33 \ln(f)$	$51.2 - 1.59 \ln(f)$	$79.0 - 2.87 \ln(f)$
1.64 $\mu\text{m}$ PZT	$45.7 - 1.07 \ln(f)$	$48.4 - 1.08 \ln(f)$	$78.8 - 2.64 \ln(f)$

When comparing to other work, such as that of Griggio et al., it is valuable to develop a sense of for the extent that device dimension and geometry have been a factor in the absolute values measured for the Rayleigh coefficients. Figure 5-7 shows how the irreversible domain wall motion was affected by the number of sections into which a membrane was broken into. The greater the number of sections, the lower the elastic restoring force for the membrane. Comparing to Table VII, a 300  $\mu\text{m}$  membrane broken into two sections has more irreversible wall motion than a 300  $\mu\text{m}$  membrane released as a “tab”, yielding an  $\alpha_0$  above 90 cm/kV. When sectioned into four segments, the  $\alpha_0$  increases to 125 cm/kV.

Figure 5-7. Effect of membrane deformation on the irreversible domain wall motion. Both  $\alpha$  and the level of dispersion increase as the restoring force for the membrane is reduced by breaking the diaphragm into more sections.

Figure 5-8. Indirectly-lit images of whole and fractured partitioned diaphragms. The cracking cracks extended to the boundary of the released region. One third of the electrode remained clamped (measured by camera software);  $\alpha$  for this region (Table VI) was separated as a linear mixing contribution.

### 5.4.3 Piezoelectric Coefficient for Membranes

The polarization and dielectric characterization of the clamped and released films has shown that domain walls are pinned less when the film is allowed to deform. This would be expected to manifest in the poling field dependences of  $e_{31,f}$  for the clamped and released structures. To assess this directly, bridges were strained by bi-axially flexing the sample; strain along the beam was measured via the strain gauge, strain in the transverse direction was measured on a separate beam with a strain gauge oriented orthogonally to the beam. The ratio of strain parallel to the beam to perpendicular to the beam was expected to be  $\sim 0.26$ , though the observed ratio was 0.44; this is likely due to additional strain from changing curvature in the uniaxially released beams. An average 3 microstrain was measured parallel to the bridges for the excitation employed. Electrodes were poled for 10 min with the drive voltage applied to the top electrode, then  $e_{31,f}$  was measured; subsequent the poling voltage sequence was repeated with progressively higher poling voltages to measure were applied to obtain the field dependence. Figure 5-9 shows the measured transverse piezoelectric coefficient for two clamped devices and two released devices. All of the  $e_{31,f}$  values were surprisingly low, given the texture of the PZT films.

Figure 5-9. The MEMS bridge structure measured the  $e_{31,f}$  of a released 1.17  $\mu\text{m}$  PZT film, the poling dependence was less steep than for a clamped (bi-layer) PZT film.

The clamped films showed a steady increase in response with poling voltage, individual electrodes grouped closely in their response. As with the field dependence of  $P_r$ , a bi-layer film structure did not result in greater de-pinning of domains than a single layer film. The released bridges however, did show a significantly larger response for low poling voltages, consistent with the trend in  $P_r$  for globally released films.

## 5.4 Conclusions

This chapter presents results of versatile electrical characterization of {001} PZT thin film membranes released by  $\text{XeF}_2$ . This method produces devices with unique which experience different mechanical boundary conditions.<sup>131,130</sup> The irreversible domain wall motion, analyzed through Rayleigh coefficients, was compared for clamped and suspended membranes, achieved by substrate undercut, and buried electrode PZT buffer layers. The Rayleigh  $\alpha$  parameter revealed that local interface clamping plays no little role in controlling the irreversible domain wall motion over the clamped film. However, a buffer layer of PZT does increase  $\alpha$ . This increase in exactly believed to be due to the thickness effect, which was shown to be strong. A thickness increase of 40% to a 1.17  $\mu\text{m}$  PZT film caused a 42% increase in  $\alpha$ .

Globally releasing the 1.17  $\mu\text{m}$  PZT film from the substrate, allowed the membrane to deform, reducing the elastic restoring force for ferroelastic domain walls. This led to a 37% increase in  $\alpha$ . Furthermore, the impact its self of relaxing stress grew with film thickness;

releasing a 1.64  $\mu\text{m}$  PZT film from the substrate yielded a 72% increase in  $\alpha$ . Local substrate release was found to have little effect other than modifying frequency dispersion for measurements at 200 kHz.

Alternatively, It was found for these samples that the remanent remanent polarization was not strongly dependant dependent on film thickness or mechanical clamping condition. As these films are MPB composition ( $c/a$  roughly  $\sim 1.02$ ), the strain energy for domain reorientation is should be modest minimum. Therefore the most likely integration into the model, substantiated by Nagarajan et al. and Wallace et al., is that it is believed that declamping from size/dimensional effects structures (single-crystal film,  $\sim 1 \mu\text{m}^3$ ) which are laterally free to deform (e.g. where the restoring forces on the domain structure are reduced) is are more effective at removing  $90^\circ$  domain wall s than declamping a feature (100's  $\mu\text{m}$  lateral polycrystalline film) from rigid clamping.<sup>93</sup> Also decreasing  $90^\circ$  domain back-switching as tetragonality decreases in *clamped* films may reconcile why back-switching was found to decrease after release for PZT 30/70 films ( $f_{001}=24\%$ ) but  $P_r$  did not increase for released PZT MPB films.

Finally, a MEMS bridge was used to measure the piezoelectric coefficient for a released thin film membrane. The wafer flexure method used a dual-purpose electrode with a piezoresistive sensitivity of  $\sim 6.2 \text{ V/strain}$ . The field dependence of  $e_{31,f}$  was in good agreement with the field dependence of  $P_r$

## Chapter 6

### Conclusion and Future Work

#### 6.1 Conclusion

This thesis pursued the optimization of PZT thin films for energy generation in self-powered MEMS. A systematic analysis of the figure of merit was made which separated the dependence of composition from the dependence of domain orientation. The  $\langle 001 \rangle$  single-domain  $e_{31}f$  for PZT thin films as a function of composition to be experimentally estimated for the first time. Chapter 3 strongly motivated the utilization of fully  $c$ -domain PZT films by demonstrating that figures of merit up to  $1 \text{ C}^2/\text{m}^4$  are attainable for (001) PZT thin films. Using MOCVD to grow PZT films on a variety of crystal substrates with tailored stress levels proved to be invaluable by removing Zr/Ti gradients, which exist at poorly characterized levels in the sol-gel films of this work. Two methods for fabricating  $c$ -domain thin film devices were then investigated in chapter 4.

Energy harvesting devices grown on MgO substrates showed that MgO is a viable substrate for fabricating released thin film devices. However, MgO was not as versatile as silicon, which can be etched rapidly by wet and dry methods. Dry (gas) etch methods were shown to be less aggressive on the interface bonding, which is tenuous between PZT films and Parylene. This prevented a thin film device from being fully released from an MgO substrate in the span of this project. The deposition of polyimide from a liquid precursor appears to solve

interface strength pitfalls which made Parylene poorly suited for wet etch release. A  $2 \text{ cm}^2$  thin film membrane was released from a silicon substrate and operated with a 5 Hz natural frequency, the lowest reported for a thin film energy harvester operating in resonant excitation. Silicon substrates facilitated scaling in size and quantity of devices compared to MgO substrates. This motivated an investigation in chapter 5 into the reduction of  $90^\circ$  domain walls for thin films released from substrate clamping conditions.

Released film test structures were designed to produce systematic changes in the clamping condition of  $\{001\}$  PZT thin films. The stiffness of the substrate interface was modified gradually by comparing a PZT buffer layer to a removed substrate from films which remained confined to the as-grown plane. This showed clearly that clamping from the thickness effect was far more influential than interface stiffness. The release of the film from the as-grown plane led to a reduction in pinning strength but a self-clamping effect remained which prevented removal of all  $90^\circ$  domain walls.

## **6.2 Future Work**

### *6.2.1 Domain Wall Back-Switching In Thin Films*

This work suggests that the maximum amount of domain reorientation in MPB PZT films after local released is comparable to that of clamped films. This behavior is in contrast to work done by Buhlmann *et al.* and Nagarajan *et al.* where finely patterned films showed increased domain wall reorientation due to declamping. One potential reason is the larger size in these PZT films.<sup>92,93</sup> Buhlmann *et al.* and Nagarajan *et al.* eliminated in-plane stress by patterning islands

with low aspect ratio ( $\sim 1:1$ ), whereas the circular membranes in this work have width:thickness ratios of  $\sim 300:1$ . Additionally, Wallace *et al.* showed a modest increase in permanent reorientation of *c*-domains substrate released for membrane structures similar to this work but using PZT 30/70 films.<sup>130</sup> This suggests that tetragonality may impart an additional dependence on the de-pinning of domain walls. The strain energy for domain reorientation in tetragonal films is higher, meaning in a clamped or released film it is costly to reorient the ferroelastic distortion. In MPB films, the barrier to irreversible domain wall motion will be lower. Potentially, the maximum amount of domain reorientation was achieved, even in clamped films. A study to track  $P_r$  with decreasing tetragonality and lateral device size would explicitly unify the three bodies of similar work and determine the relative requirements for total removal of  $90^\circ$  domain walls. Substrate (global) release has been shown effective in relaxing in-plane stress, it may also produce differences in absolute critical de-clamping size. Islands patterned on rigid substrates were effectively clamped after a mere 10:1 geometry; this would be an unfortunate upper limit in aspect ratio for achieving total  $90^\circ$  domain wall removal.

### 6.2.2 Thin Film Transfer From Arbitrary Substrates

The transfer of PZT films to flexible membranes has received increased attention in literature, especially due to the potential applications for MEMS sensors and energy harvesters. The methods in this work employed aggressive acid solutions and/or exotic (and slow) vapor etch methods to dismantle the relatively strong interface which forms from thin film growth. Previous Other authors had reported good better success with acid undercutting of the film and

or even laser ablation exfoliation of the interface.<sup>122</sup> One way to facilitate the release of PZT thin films is would be to make the a sacrificial interfacial material susceptible to gentle etchants. This could be done, for example, such as using thin film ZnO, which can readily be removed is ton acetic acid. This material can be deposited by ALD on large areas and allows for an attractive means to release large areas in parallel. PZT deposited by sol-gel on Pt/ZnO/SiO<sub>2</sub>/Si substrates represent a relatively economic route to produce released PZT film membranes. This fabrication method is also well suited to investigate properties of released films, such as the experiments suggested in this chapter.

### *6.2.3 Integrated ZnO TFT Electronics on PZT Devices*

Active switching circuitry can bring significant gains to vibration power harvesting by removing the parasitic threshold voltages in solid state rectifiers and by optimizing the circuit impedance, ; a 500% increase in transferred power over a traditional diode bridge was reported using the double synchronous switch method. Rectification circuitry would ideally be integrated onto the piezoelectric MEMS, which are not necessarily CMOS devices. ZnO thin film transistors are very good candidates for this task and their fabrication has been recently demonstrated on PZT films. A ZnO double gate TFT rectifier was demonstrated by Sun et al.; it recently and did consumed less energy than would be lost from from conventional p-n Schottky diodes. Low frequency vibration harvesting is particularly appropriate for ZnO switches, which consume more power as desired switching frequency increases. A PZT thin film energy harvester co-processed with integrated rectification circuitry would be easily integrated into a power

system for MEMS. If the TFTs are deposited on the beam, then this endeavor requires the membrane lift-off to be performed last. This suggests the thin films would most likely be released by acetic acid dissolution of a ZnO interface,  $\text{XeF}_2$  substrate undercut, or by using a highly flexible substrate such as thin Ni foil.

## Appendix A

### Thin Film Composites for Energy Harvesting

With the intent of optimizing a piezoelectric thin film for energy harvesting, the properties of 2-2 and 3-2 piezoelectric composites were investigated. Finite element analysis (FEA) models for laminar composites found that a 2-2 composite of PMN-PT and  $\text{Al}_2\text{O}_3$  enables a figure of merit up to 2.5 times larger than the base PMN-PT composition. It was also predicted that *no* composite geometry for PZT and  $\text{Al}_2\text{O}_3$  produced an increase in figure of merit due to the lower coupling coefficient of PZT compared to single-crystal PMN-PT.

#### A.1 Introduction

Generally as  $e_{31,f}$  increases, so does the dielectric constant. This natural tendency is unfavorable for the figure of merit. The intent of this work is to combine a low dielectric constant and high piezoelectric coefficient. Composite piezoelectrics allow connectivity to be used as a design tool to control the distribution of mechanical and electrical fields. This work uses FEA and analytic models to predict the figure of merit of composite films for MEMS energy harvesting. Thin film  $\text{Al}_2\text{O}_3$ /PZT bilayers were fabricated for comparison, 2-2 and 3-2 lamellar

composites were chosen due to the relative ease of fabrication. Although 2-2 composites have been used to increase the bulk hydrophone transducer figure of merit, they have not been used with the passive and active phases electrically in series, as is done here.

## A.2 Procedure

### Modeling of Composites

The finite element analysis (FEA) modeling suite PZFlex was used to build models of piezoelectric composites and predict elastic, electrical and piezoelectric behavior. Data for PZT4 and PMN-30PT from the PZFlex database were used to compare behavior of different piezoelectrics; ceramic alumina was used for the low permittivity material. The full property sets used for the three materials is given in Table A.

Table A. Material Properties Used in Modeling

	$e_{31}$	$e_{33}$	$e_{15}$	$e_{31,f}$	
	C/m <sup>2</sup>	C/m <sup>2</sup>	C/m <sup>2</sup>	C/m <sup>2</sup>	
PZT4	-3.0	16.7	11.4	-13.26	
PMN-30PT	-3.9	20.3	12.7	-24.00	
	$c_{11}^E$	$c_{12}^E$	$c_{13}^E$	$c_{33}^E$	$c_{44}^E$
	GPa	GPa	GPa	GPa	GPa
PZT4	147	81.1	81.1	132	31.3

PMN-30PT	115	103	102	103	69.0
Al <sub>2</sub> O <sub>3</sub>	468	142	142	468	153
	$\epsilon_{33,r}^X$	$\epsilon_{33,r}^x$	$\epsilon_{11,r}^x$	$k_{31}$	
PZT4	1183	635	730	-0.298	
PMN-30PT	9280	680	1434	-0.614	
Al <sub>2</sub> O <sub>3</sub>	8	8	8	0	

A two dimensional model of a lamellar composite material was made in PZFlex, which consisted of two materials that are mechanically coupled and electrically in series. In calculating the piezoelectric response, the charge developed on the electrodes was determined when a static pressure load was applied to strain the composite. Mechanical symmetry boundaries kept the body from accelerating while remaining unclamped on all sides. Figure A-1 depicts the model of a 2-2 composite. The effective piezoelectric coefficient  $e_{31,f}$  of the composite is calculated by dividing the charge calculated on the electrodes in the 3-axis by the strain in the 1-axis. Free permittivity is calculated by applying an electric field in the 3-axis. The resulting charge is calculated on the electrodes and the capacitance of the body is obtained by  $C=Q/V$ .

Fig A-1. Schematic of 2-D PZFlex model for a 2-2 composite.

The first set of calculations were undertaken to compare the finite element model with reported analytic solutions for the properties of 2-2 piezoelectric composites from Topolov and

Turik (2000). The  $e_{31,f}$  coefficient was obtained from the Topolov and Turik solutions by. Models were also constructed to describe 3-2 connectivity, in which the low permittivity layer is not continuous (such that the area coverage fraction of the  $\text{Al}_2\text{O}_3$  region was varied between 0 and 1). Figure A-2 shows a schematic of the PZT4/ $\text{Al}_2\text{O}_3$  3-2 composite.

### Composite Thin Film Deposition

PZT ( $\text{Zr}=0.52$ ,  $\text{Ti}=0.48$ ) thin films were deposited on Pt/Ti/ $\text{SiO}_2$ /Si substrates (NOVA Electronic Materials) by chemical solution deposition and crystallized by rapid thermal anneal (RTA) at  $700^\circ\text{C}$  for 60 sec. The final thicknesses varied between 1.2-0.85  $\mu\text{m}$ . Films deposited on Pt had either random or slight (111) texture, a lead titanate buffer layer was used to achieve ( $\{100\}$ ) texture. Deposition of 3-30 nm of amorphous  $\text{Al}_2\text{O}_3$  was done by sputtering or plasma enhanced atomic layer deposition (PEALD). The thickness was limited to 3-30 nm because 2-2 composites with more than 5%  $\text{Al}_2\text{O}_3$  were unable to be poled without electric breakdown. It was found in a different experiment that only  $\text{Al}_2\text{O}_3$  on the top surface of the PZT film retained useful dielectric properties (i.e. buried  $\text{Al}_2\text{O}_3$  reacted during the crystallization step) so multiple alternating layers could not conveniently be prepared. Therefore the samples are bi-layer composites.

$\text{Al}_2\text{O}_3$  was deposited by RF magnetron reactive sputtering (Lesker CMS-18 Sputter Tool) at

room temperature from an Al metal target 12 cm away from the sample. The deposition parameters are shown in Table B. One condition includes a forward power applied to the sample and is referred to here as “sputtered with bias”. The oxygen plasma pre-cleaning step is also shown.

Table B. Al<sub>2</sub>O<sub>3</sub> Sputter Deposition Conditions

Target Power	Substrate Power	Pressure	O <sub>2</sub> %	Rate
200 W	0 W	5.0 mtorr	10	3.33 Å/min
300 W	7 W	5.0 mtorr	12.5	6.0 Å/min
0 W	10 W	25 mtorr	100	60 s Clean

Thin film bilayers with 3-2 connectivity were fabricated by patterning lines in photoresist (Shipley 1811) on the PZT, followed by an O<sub>2</sub> plasma clean and the Al<sub>2</sub>O<sub>3</sub> deposition at 3.33 Å/min. The photo resist was then removed by sonicating in acetone and cleaned by O<sub>2</sub> plasma before top electrodes were deposited. This resulted in a known ratio of area under each electrode which did (and did not) have Al<sub>2</sub>O<sub>3</sub>. Lines with four different dimensions were patterned to examine the effect of different coverage ratios. Table C shows the width of the Al<sub>2</sub>O<sub>3</sub> lines forming the 3-2 composite films.

Table C. Al<sub>2</sub>O<sub>3</sub> Lines with Percent Coverage

Area Al <sub>2</sub> O <sub>3</sub>	91%	80%	67%	50%
-------------------------------------	-----	-----	-----	-----

Al <sub>2</sub> O <sub>3</sub> Width (μm)	100	100	50	50
PZT Exposed (μm)	10	25	25	50

Al<sub>2</sub>O<sub>3</sub> was deposited by PEALD at 200°C at a rate of 0.15 nm/cycle, using trimethylaluminum as the Al source and CO<sub>2</sub> as the carrier gas and oxidant as described elsewhere. Platinum top electrodes (500 nm) were deposited through a shadow mask and annealed by RTA at 550°C in O<sub>2</sub> for 60 s.

#### Electric and Piezoelectric Characterization

Capacitance was measured on an LCR bridge (HP 4192A) and was compared to the effective capacitance calculated from series capacitors. Hysteresis loops were taken (Radiant Radiant Tech. RT-66) to find the effect of Al<sub>2</sub>O<sub>3</sub> thickness on remanent polarization and coercive field.

The piezoelectric coefficient  $e_{31,f}$  was measured using a wafer flexure tool.

### **A.3 Results and Discussion**

#### Modeling 2-2 Piezoelectric Composites

The PZFlex model predicted the effective  $e_{31,f}$  of 2-2 composites with good agreement to the analytic solutions from Topolov and Turik. The only coefficient which did not agree with the analytic solution was the composite effective stiffness coefficient  $c_{33}$ . Figure A-2 shows  $c_{33}$  as a function of PZT volume fraction calculated by (5) and by PZFlex.

(5)

The PZFlex model reveals that between 100% and 90% PZT, piezoelectric stiffening results in a transition from stiffness at constant field to stiffness at constant charge within the PZT phase. This automatic treatment of stiffness and permittivity as functions of electrical boundary conditions present a strength of the FEA approach over an analytic one.

Fig A-2. FEA and analytic predictions for PZT4/Al<sub>2</sub>O<sub>3</sub> composite  $c_{33}$ .

The piezoelectric coefficient  $e_{31,f}$  and the relative free permittivity  $\epsilon_r^X$ , of the 2-2 composites with up to 5% Al<sub>2</sub>O<sub>3</sub> are shown in Figure A-3. For both cases,  $e_{31,f}$  drops at similar rates with the addition of Al<sub>2</sub>O<sub>3</sub> while the dielectric constant falls much more rapidly for

the composite with PMN-PT. Figure A-4 shows the resulting increase in the energy harvesting figure of merit, which maximized at 248% of the pure PMN-PT.

a)

b)

Fig A-3. a) Normalized  $e_{31,f}$  and, b) normalized permittivity

Fig A-4. FoM predicted by FEA and Topolov and Turik, comparing PZT4 and PMN-PT.

No increase in the figure of merit was predicted for the PZT composite. The maxima shown in Figure A-4 for the PMN-PT/ $\text{Al}_2\text{O}_3$  composite is due to an increase in the piezoelectric voltage coefficient,  $h_{31,f}$ , due to a rapid reduction in the effective dielectric constant as the alumina thickness increases. It was found that the clamped permittivity of the phases was primary in controlling the rate at which the series piezoelectric coefficient decreased. The clamped permittivity of PMN-PT and PZT is nearly equal, so  $e_{31,f}$  decreases at nearly equal rates with  $\text{Al}_2\text{O}_3$  coating, as seen in Figure A-4 a). Conversely, it is the free permittivity of the two phases which controls the decrease in the composite permittivity, which appears in the denominator of the figure of merit. The higher free permittivity of PMN-PT causes a much more

rapid decrease than in the case of PZT4, as shown in Figure 5 b). In general, the difference in the free and clamped permittivity of materials is described by equation 6.

$$(6)$$

This difference is large when materials have a high  $d_{31}$  coefficient and a low  $s_{11}$  coefficient. In other words, the difference between free and clamped permittivity will be high when the material has a high  $k_{31}$  coupling coefficient. The coupling coefficient of the PZT4 is too small to provide an increase the figure of merit for a 2-2 composite with alumina. Increasing the clamped permittivity of the PZT4 caused  $e_{31,f}$  to fall more rapidly while increasing the permittivity of the  $\text{Al}_2\text{O}_3$  caused  $e_{31,f}$  to fall less rapidly.

### $\text{Al}_2\text{O}_3$ /PZT Thin Film Bilayers

To test the models developed, the piezoelectric and dielectric properties of bilayer composites were measured and compared to the figure of merit versus thickness of  $\text{Al}_2\text{O}_3$ . Figure A-5 shows the hysteresis loops for bilayer films with various thicknesses of PEALD deposited  $\text{Al}_2\text{O}_3$ . Since the dielectric constant of the  $\text{Al}_2\text{O}_3$  is substantially lower than the PZT, ~8 and 1100 respectively, field is not constant across the composite. It was found that the coercive voltage of the bilayer increases approximately linearly as  $\text{Al}_2\text{O}_3$  is added. This is in agreement

with the work of Jiang *et al.* [33].

Fig A-5. Hysteresis loops of Al<sub>2</sub>O<sub>3</sub>/ PZT bilayer films

The permittivity versus Al<sub>2</sub>O<sub>3</sub> thickness is shown in Figure A-6 and is in good agreement to the expected value for capacitors in series calculated from (6). In contrast,  $\epsilon_{31,f}$  of the bilayers was consistently higher than the values predicted from Topolov & Turik and PZFlex (Figure A-7). This led to a shallow increase in the figure of merit observed from 0-2% Al<sub>2</sub>O<sub>3</sub>, or 0-20 nm in Figure A-8. There was also an apparent difference based on the method of the deposition. Specifically,  $\epsilon_{31,f}$  for sputtered films often exceeded that of the PEALD films for a given alumina thickness, resulting in a higher figure of merit. Figure 10 shows a normalized figure of merit for similar depositions of Al<sub>2</sub>O<sub>3</sub> but onto (100) textured PZT films. The result is similar, showing a slight increase in figure of merit with higher values for the sputtered Al<sub>2</sub>O<sub>3</sub>. Though Because a monotonic decrease in the figure of merit is predicted for a 2-2 composite of PZT and Al<sub>2</sub>O<sub>3</sub>, it is believed that the anomalous behavior could be explained by a 3-2 connectivity.

Fig A-6. Measured dielectric constant of bilayer composites compared to Equation (6).

Fig A-7. Measured  $e_{31,f}$  of bilayer composites with random PZT, bars represent standard deviation of charge measurements on multiple electrodes.

Fig A-8. FoM:  $(e_{31,f})^2/\epsilon_r$  of bilayer composites with a randomly oriented PZT film.

#### A.4 Summary

A FEA model was used to predict dielectric and piezoelectric properties of composites with arbitrary geometry, the model was in excellent agreement with analytic solutions for 2-2 composites. It was shown that a series 2-2 composite is beneficial for MEMS energy harvesting when the piezoelectric coupling coefficient is high. An optimized composite with  $\text{Al}_2\text{O}_3$  and PMN-30PT was predicted to have a figure of merit 248% higher than the pure material. 2-2 composites using PZT did not have a predicted increase in figure of merit. Nonetheless, but bilayer thin films with less than 20 nm of  $\text{Al}_2\text{O}_3$  did might show minor increases in the figure of merit, though uncertainty in piezoelectric coefficient imparts difficulty in producing means that the changes are typically within the accuracy of the measurements precision.



## REFERENCES